

Clustering of quasars in SDSS-IV eBOSS: study of potential systematics and bias determination

This content has been downloaded from IOPscience. Please scroll down to see the full text.

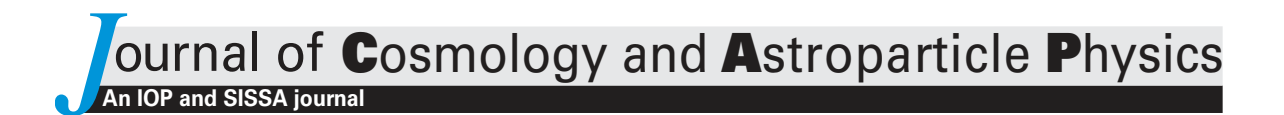
View the table of contents for this issue, or go to the journal homepage for more

Download details:

IP Address: 136.152.227.131

This content was downloaded on 10/08/2017 at 20:45

Please note that terms and conditions apply.



# Clustering of quasars in SDSS-IV eBOSS: study of potential systematics and bias determination

Pierre Laurent,<sup>a</sup> Sarah Eftekharzadeh,<sup>b</sup> Jean-Marc Le Goff,<sup>a,1</sup> Adam Myers,<sup>b</sup> Etienne Burtin,<sup>a</sup> Martin White,<sup>c,d,e</sup> Ashley J. Ross,<sup>f</sup> Jeremy Tinker,<sup>g</sup> Rita Tojeiro,<sup>h</sup> Julian Bautista,<sup>i</sup> Jonathan Brinkmann,<sup>j</sup> Johan Comparat,<sup>k</sup> Kyle Dawson,<sup>i</sup> Hélion du Mas des Bourboux,<sup>a</sup> Jean-Paul Kneib,<sup>l</sup> Ian D. McGreer,<sup>m</sup> Nathalie Palanque-Delabrouille,<sup>a</sup> Will J. Percival,<sup>n</sup> Francisco Prada,<sup>o</sup> Graziano Rossi,<sup>p</sup> Donald P. Schneider,<sup>q</sup> David Weinberg,<sup>r</sup> Christophe Yèche ,<sup>a</sup> Pauline Zarrouk<sup>a</sup> and Gong-Bo Zhao<sup>s</sup>

<sup>&</sup>lt;sup>a</sup>IRFU, CEA, Université Paris-Saclay, F-91191 Gif-sur-Yvette, France

<sup>&</sup>lt;sup>b</sup>Department of Physics and Astronomy, University of Wyoming, Laramie, WY 82071, U.S.A.

<sup>&</sup>lt;sup>c</sup>Lawrence Berkeley National Lab, 1 Cyclotron Rd, Berkeley CA 94720, U.S.A.

<sup>&</sup>lt;sup>d</sup>Department of Physics, University of California, Berkeley, CA 94720, U.S.A.

<sup>&</sup>lt;sup>e</sup>Department of Astronomy, University of California, Berkeley, CA 94720, U.S.A.

<sup>&</sup>lt;sup>f</sup>Center for Cosmology and AstroParticle Physics, The Ohio State University, Columbus, OH 43210, U.S.A.

 $<sup>^</sup>g{\rm Center}$  for Cosmology and Particle Physics, Department of Physics, New York University, New York, 10003, U.S.A.

<sup>&</sup>lt;sup>h</sup>School of Physics and Astronomy, North Haugh, St. Andrews KY16 9SS, U.K.

<sup>&</sup>lt;sup>i</sup>Department of Physics and Astronomy, University of Utah, Salt Lake City, UT 84112, U.S.A.

<sup>&</sup>lt;sup>j</sup>Apache Point Observatory, P.O. Box 59, Sunspot, NM 88349, U.S.A.

<sup>&</sup>lt;sup>k</sup>Max-Planck-Institut für Extraterrestrische Physik, Giessenbachstraße, 85748 Garching, Germany

 $<sup>^</sup>l {\rm Laboratoire}$  d'Astrophysique, École Polytechnique Fédérale de Lausanne, 1015 Lausanne, Switzerland

<sup>&</sup>lt;sup>m</sup>Steward Observatory, University of Arizona, Tucson, AZ 85721–0065, U.S.A.

<sup>&</sup>lt;sup>1</sup>Corresponding author.

- <sup>n</sup>Institute of Cosmology and Gravitation, University of Portsmouth, Dennis Sciama building, PO1 3FX, Portsmouth, U.K.
- <sup>o</sup>Instituto de Fìsica Teórica (IFT) UAM/CSIC, Universidad Autónoma de Madrid, Cantoblanco, E-28049 Madrid, Spain
- <sup>p</sup>Department of Astronomy and Space Science, Sejong University, Seoul, 143-747, Korea
- <sup>q</sup>Institute for Gravitation and the Cosmos, Pennsylvania State University, University Park, PA 16802, U.S.A.
- <sup>r</sup>Department of Physics and Center for Cosmology and AstroParticle Physics, The Ohio State University, Columbus, OH 43210, U.S.A.
- <sup>s</sup>National Astronomical Observatories of China, Beijing 100012, China

E-mail: jmlegoff@cea.fr

Received May 16, 2017 Accepted June 27, 2017 Published July 11, 2017

**Abstract.** We study the first year of the eBOSS quasar sample in the redshift range 0.9 < z < 2.2 which includes 68,772 homogeneously selected quasars. We show that the main source of systematics in the evaluation of the correlation function arises from inhomogeneities in the quasar target selection, particularly related to the extinction and depth of the imaging data used for targeting. We propose a weighting scheme that mitigates these systematics. We measure the quasar correlation function and provide the most accurate measurement to date of the quasar bias in this redshift range,  $b_Q = 2.45 \pm 0.05$  at  $\bar{z} = 1.55$ , together with its evolution with redshift. We use this information to determine the minimum mass of the halo hosting the quasars and the characteristic halo mass, which we find to be both independent of redshift within statistical error. Using a recently-measured quasar-luminosity-function we also determine the quasar duty cycle. The size of this first year sample is insufficient to detect any luminosity dependence to quasar clustering and this issue should be further studied with the final  $\sim 500,000$  eBOSS quasar sample.

**Keywords:** galaxy clustering, redshift surveys, cosmological parameters from LSS

**ArXiv ePrint:** 1705.04718

$\mathbf{C}$	ontents				
1	Introduction	1			
2	Data sample	3			
	2.1 eBOSS survey				
	2.2 Quasar selection	-			
3	Analysis				
	3.1 Computing $\xi(r)$	4			
	3.2 Estimation of statistical uncertainties	(			
4	Systematic effects				
	4.1 Inhomogeneities of target identification	7			
	4.2 Inhomogeneities of quasar target selection	8			
	4.3 Effect of weightings on $\xi(r)$	10			
5	Measurement of the quasar bias	10			
6	The halo mass and the duty cycle of eBOSS quasars				
	6.1 Characteristic Halo Mass	13			
	6.2 Duty cycle	15			
7	Conclusion	17			

### 1 Introduction

The best current constraints on the cosmological parameters are from the power spectrum of temperature fluctuations [1–5] in the Cosmic Microwave Background (henceforth CMB). In this regard, the latest Planck satellite results provide overwhelming evidence for non-zero cosmic acceleration or "dark energy" with  $\Omega_{\rm DE}=0.692\pm0.012$  [6]. The CMB, however, can only provide a measurement at one redshift (the epoch of the surface of last scattering at  $z\sim1100$ ), and, so, measurements across many redshifts are required to constrain the equation of state of dark energy [7–9]. As galaxies and quasars occupy a three-dimensional web that traces a range of redshifts, they offer a unique probe of the evolution of dark energy over more than 10 billion years of cosmic history. Cosmological experiments are thus, increasingly, turning in part to vast redshift surveys in an attempt to map the Universe in order to specifically study dark energy through the growth of structure [10–14].

The first significant galaxy redshift surveys [15–17], were improved upon by surveys such as the 2dF Galaxy Redshift survey [18], the DEEP2 survey [19] and the Sloan Digital Sky Survey (henceforth SDSS; [20]) "main" galaxy sample [21] and Luminous Red Galaxy (henceforth LRG) sample [22]. The use of galaxies from such surveys as tracers at significantly lower redshifts than the CMB have helped to precisely pin down our cosmological world model [23–28]. In particular, such surveys have been used to measure the influence of baryons on galaxy clustering [29] and to confirm the potential use of baryon-driven fluctuations (so-called Baryon Acoustic Oscillations, or BAOs) in the galaxy power spectrum as a standard ruler with which to set the cosmological distance scale [30].

The realization that essentially every galaxy hosts a supermassive black hole [31–34], and that a quasar is therefore just a phase in the normal cycle of a galaxy, prompted the more general use of quasars as cosmological tracers. Recent major redshift surveys have also, therefore, used quasars to probe large-scale structure, with the 2dF QSO Redshift Survey [35] and the Sloan Digital Sky Survey (SDSS) quasar surveys [36, 37] being notable examples. Quasar redshift surveys have often operated in tandem with galaxy surveys, and have highlighted the possibility of using quasars to constrain cosmology at higher redshifts than would be possible for galaxy samples to similar magnitude limits [38–40].

In addition to probing cosmology, quasar clustering can be used as a tool to constrain the interplay of supermassive black holes, galaxies, and dark matter halos, and how that interplay evolves with cosmic time. Measuring the bias of quasars constrains the mass of the dark matter halos that quasars occupy. In turn, measuring the abundance of such halos compared to the number density of the quasars they host can begin to constrain the duration of the quasar phase. In general, this has led to a consistent picture where UV/optically luminous quasars are biased by a factor of  $b_{\rm Q}\sim 2$  at redshift  $z\sim 1$  rising to  $b_{\rm Q}\sim 3$  at  $z\sim 2$  and  $b_{\rm Q}>4$  at z>3 [41–49]. This implies that UV/optically luminous quasars at z<2.5 are hosted by halos with an average mass of a few times  $10^{12}\,h^{-1}M_{\odot}$  and are "on" for a few per cent of the Hubble time. Precise bias and mass measurements for UV/optically luminous quasars at multiple redshifts are crucial in helping to tie down the role of quasars in galaxy evolution (see, e.g., [50] for an overview). In particular, the ties between quasars and star-formation signatures are increasingly being analyzed by measuring the clustering of quasars selected across the electromagnetic spectrum [51–60].

As clustering measurements have become increasingly precise, they have become dominated by systematics. Some systematics arise from per-cent-level imperfections in calibrating the target imaging or survey spectroscopy that are critical to assembling large redshift catalogs. Other common systematics include contamination by non-cosmological sources such as stars, or general foregrounds such as Galactic dust. Such systematics can be scale-dependent, affecting not just the amplitude of clustering measurements, but also the overall shape of the power spectrum of tracers. Obviously, this can be a concern for both cosmological constraints and for characterizing the dark matter halos occupied by tracer populations. To counter this, procedures have been developed to calculate weighting maps and exclusion masks to ameliorate clustering systematics both for galaxies [61–63] and for quasars [64–69].

The Baryon Oscillation Spectroscopic Survey (BOSS; [12]) conducted as part of the third iteration of the SDSS [70] focused on using quasars and galaxies as complementary probes of a BAO feature at  $\sim 100\,h^{-1}\,\mathrm{Mpc}$  in order to calibrate the redshift-distance relation. At redshifts of z < 0.7, galaxies were used as direct tracers of the matter power spectrum [71–73] and at z > 2.1 clouds of neutral hydrogen in the Lyman- $\alpha$  Forest, as illuminated by background quasar-light, were similarly used [74–78]. Beyond its cosmological impact, BOSS provided by far the most precise constraints on the bias and host-halo-masses of quasars at  $z \sim 2.5$  [48, 49]. The success of BOSS led to the development of an extended spectroscopic redshift survey using the SDSS telescope (extended-BOSS or eBOSS; [14]). The cosmological goal of eBOSS [79] is to detect the  $\sim 100\,h^{-1}\,\mathrm{Mpc}$  BAO scale in redshift ranges not yet probed by spectroscopic surveys; LRGs at 0.7 < z < 0.9 [80]; Emission Line Galaxies at  $z \sim 0.9$  [81, 82] and quasars at 0.9 < z < 3.5 [83]. In addition eBOSS will attempt to improve BAO constraints by identifying new quasars to trace the Lyman- $\alpha$  Forest [84].

Ultimately, eBOSS will provide over half-a-million spectroscopically confirmed quasars at redshifts of z > 0.9 [83]. This sample will provide an unparallelled opportunity to study

galaxy evolution and the BAO scale through quasar clustering, particularly with careful control of the systematics that can contaminate clustering measurements. In this paper, we present measurements of quasar clustering using the first year of eBOSS observations. The sample that we analyze approaches 70,000 optically luminous quasars in the redshift range 0.9 < z < 2.2. Even after only its first year, eBOSS has spectroscopically confirmed  $\sim 2-3$  times as many 0.9 < z < 2.2 quasars as used in the main clustering analyses of the 2dF QSO Redshift Survey and the SDSS-I/II [41, 46, 47]. In this paper, we focus on correcting for the systematics and inhomogeneities that can contaminate eBOSS clustering measurements. We measure the evolution of quasar bias with unprecedented precision. We then interpret our bias measurements in terms of the characteristic masses of quasar-hosting halos, and estimate the duty cycle of quasars at 0.9 < z < 2.2. A companion paper [85] reexamines our analyses in the context of sophisticated N-body simulations.

## 2 Data sample

# 2.1 eBOSS survey

The six years of observations of eBOSS [14] started in July 2014. At the end of the survey a sample of more than 500,000 spectroscopically confirmed quasars will be available over 7500 deg<sup>2</sup> in the redshift range 0.9 < z < 2.2. This will allow for a measurement of the BAO scale and provide measurements of the angular diameter distance,  $d_A(z)$ , and of H(z) to a 2.8% and a 4.2% accuracy, respectively [79]. The program also includes 250,000 new luminous red galaxies (LRG) at  $\langle z \rangle = 0.72$ , to be combined with BOSS LRGs and 195,000 emission-line galaxies at  $\langle z \rangle = 0.87$ . Finally the spectra of 60,000 new quasars at z > 2.1 will be measured and the spectra of 60,000 known quasars at z > 2.1 will be remeasured to improve their signal-to-noise ratio. This will improve BOSS Lyman- $\alpha$  BAO measurement.

The program makes use of upgraded versions of the SDSS spectrographs [86] mounted on the Sloan 2.5-meter telescope [87] at Apache Point Observatory, New Mexico. An aluminum plate is set at the focal plane of the telescope with a 3° diameter field-of-view. Holes are drilled in the plate, corresponding to 1000 targets, i.e., objects to be observed with one of the two spectrographs. An optical fiber is plugged to each hole and links to the spectrographs. The minimum distance between two fibers on the same plate corresponds to 62" on the sky, which results in some "collisions" between targets. It may, however, be possible to observe both colliding targets if they are in the overlap region between two or more plates.

## 2.2 Quasar selection

The eBOSS quasar selection [83] involves a homogeneous CORE selection that combines an optical selection in (u,g,r,i,z) bands, using a likelihood-based routine called XDQSOz, with a mid-IR-optical color cut. The extreme deconvolution (XD) algorithm<sup>1</sup> was applied in BOSS to model the distributions of quasars and stars in flux space, and hence to separate quasar targets from stellar contaminants (XDQSO; [89]). In eBOSS we use the XDQSOz extension [90], which selects quasars in any specified redshift range. We start from the SDSS photometric images in 5 bands (u,g,r,i,z) [91] with updated calibration of SDSS imaging relative to BOSS [92]. We select point sources with deextincted PSF magnitudes g < 22 or

<sup>&</sup>lt;sup>1</sup>XD [88] is a method to describe the underlying distribution function of a series of points in parameter space (e.g., quasars in color space) by modeling that distribution as a sum of Gaussians convolved with measurement errors.

r < 22 that have an XDQSOz probability P(z > 0.9) > 0.2. This selection includes quasars at z > 2.2, which are not used for direct quasar clustering but for Lyman- $\alpha$  forest studies. There is another quasar selection in eBOSS dedicated to z > 2.2 Lyman- $\alpha$  quasars, with an average 20 targets per deg<sup>2</sup>. We do not discuss it here.

In contrast to quasars, stars tends to be dim in the mid-IR wavelengths. We make a weighted average of the WISE [93] w1 and w2 mid-IR fluxes to optimize the S/N ratio and similarly a weighted average of SDSS g, r and i PSF fluxes. Selecting targets with a resulting average optical magnitude significantly larger than the IR magnitude such that  $m_{\rm opt} - m_{\rm IR} \ge (g-i) + 3$ , reduces the star contamination in our sample without significantly removing quasars.

This selection results in an average 115 targets per  $\deg^2$ , out of which 25 have already been observed by SDSS I, II or III, so there remain 90 targets per  $\deg^2$  to be measured by eBOSS. These 25 and 90 targets per  $\deg^2$  result, respectively, in 13 quasars per  $\deg^2$  that we call "known quasars" and 58 new quasars per  $\deg^2$  that we call "eBOSS quasars", in both case in the range 0.9 < z < 2.2. This makes a total of about 70 quasars per  $\deg^2$  and matches the requirement to reach a 2% accuracy on the BAO scale [14].

Part of the eBOSS footprint was observed by SEQUELS [14, 83], a pilot survey at the end of SDSS III. SEQUELS differs from the rest of eBOSS survey in two ways: the apatial placement of the plates was denser, one plate per  $\approx 4~\rm deg^2$  instead of one plate per  $\approx 5~\rm deg^2$ , and all quasar-target spectra were visually inspected. The first difference is taken into account by the completeness (see section 3.1) and, in order to treat them as all eBOSS quasars, we use only the pipeline information for SEQUELS quasars.

The data used in this paper include all spectra taken during the first year of eBOSS data taking, up to July 2015. They cover a surface of 1200 deg<sup>2</sup>.

# 3 Analysis

#### 3.1 Computing $\xi(r)$

There are a limited number of fibers available so all targets cannot be ascribed a fiber and observed. Since the density of eBOSS targets is not homogeneous, their probability to be observed is not homogeneous either. In addition targets are more likely to be observed when located on areas where plates overlap. In order to take those effects into account we define polygons as the intersections of the plates projected on the celestial sphere, and in each polygon we define a completeness

$$C = \frac{N_{\text{obs}} + N_{\text{col}}}{N_{\text{targets}} - N_{\text{known}}}.$$
(3.1)

Here  $N_{\rm obs}$  is the number of observed targets,  $N_{\rm targets}$  the total number of targets,  $N_{\rm known}$  the number of targets that have already been observed by the SDSS I, II and BOSS surveys, and  $N_{\rm col}$  is the number of targets that were not observed because they are colliding with a quasar. Known targets are not re-observed by eBOSS in order to save fibers, and are thus removed from the denominator of equation (3.1). Besides, known target completeness is by definition equal to 1, which would bias our measurement. In order to force the known-target completeness to be the same as for other targets, we remove some known targets from the sample with a survival probability equal to the value of the completeness in their polygon. We account for collisions as in Anderson et al. [94]: when a target is not observed due to collision, we upweight by one unit the closest observed quasar within 62". Therefore we

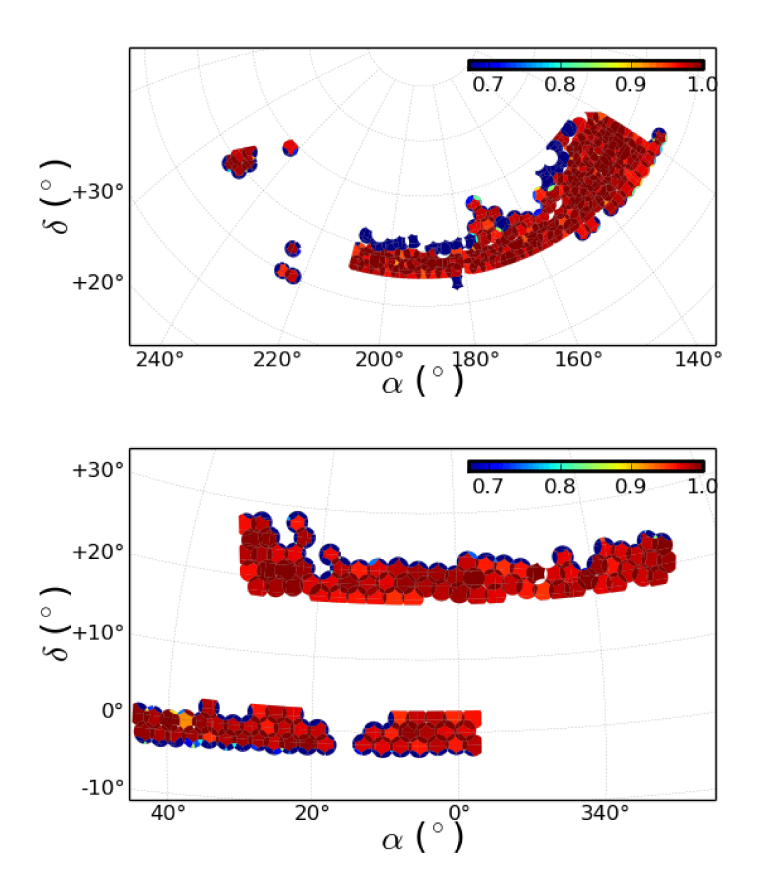


**Figure 1.** Angular distribution of the selected data in the NGC (left) and the SGC (right). The color scale indicates the survey completeness in each polygon.

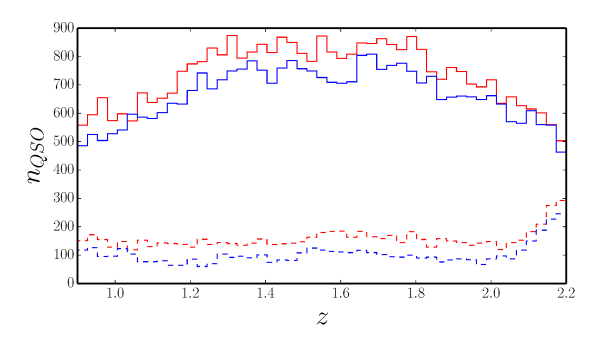


**Figure 2**. Redshift distribution of eBOSS quasars (continuous line) and known quasars (dashed line) in the NGC (red) and SGC (blue).

add these collided targets to the numerator when computing the completeness. If there is no quasar within 62", this target is treated as any other unobserved targets. However, this method supposes that the redshift of the collided target and the upweighted quasar is the same. Bianchi and Percival [95] extensively discuss the biases and the limitations of the different methods used in the litterature to account for collisions. They present an unbiased weighting scheme done at the pair level, which uses the observed closed pairs located on overlapping plates. However, since we only focus on scales larger than 10 Mpc in this

analysis, we decide to keep the simpler upweighting scheme to handle collisions. Figure 1 shows the completeness of the eBOSS survey in the North Galactic Cap (NGC) and South Galactic Cap (SGC), as computed with the Mangle software [96].

To correct for completeness, we generate a catalog of  $10^7$  objects with "random" angular positions over the eBOSS footprint, with the number of random objects in each polygon proportional to its area times its completeness. We then assign to each random object a redshift that is drawn from the measured redshift distribution n(z), see figure 2. Finally, we compute  $\xi(r)$  with the Landy-Szalay estimator [97]:

$$\hat{\xi}^{LS}(r) = \frac{dd(r) - 2dr(r) + rr(r)}{rr(r)}, \qquad (3.2)$$

where dd(r) is the number of pairs of quasars separated by a distance r, dr(r) is the number of pairs between a quasar and an object from the random catalog, and rr(r) the number of pairs of random objects. These three quantities are normalized to the total number of pairs.

As mentioned in section 2, the measure of the correlation function  $\xi(r)$  is very sensitive to inhomogeneities in the quasar target selection. We apply veto masks to remove from our sample all quasars and random objects that are located in areas where the target selection is too contaminated to be modelled and easily corrected. These areas include regions around bright objects (stars or galaxies) and where the SDSS photometry is unreliable. These veto masks correspond to the masks used for BOSS DR12 [98]. We also remove areas covered by the centerpost of the eBOSS plates, since we cannot observe those areas.

#### 3.2 Estimation of statistical uncertainties

We compare two methods to compute covariance matrices. The first method, developed by Laurent et al. [69], uses bootstrap realizations. For each galactic cap, we define 201 rectangular bootstrap cells with identical effective volume. We obtain a bootstrap realization by drawing 201 cells with replacement from the 201 bootstrap cells, and compute  $\xi(r)$  for this realization. We repeat this operation 10,000 times, and estimate the covariance matrix of  $\xi(r)$  from the covariance of  $\xi(r)$  for these 10,000 realizations. Bootstrap resampling ignores cosmic variance, but this is not an issue here since our sample is shot-noise limited. Finally, we note that computing the covariance matrix from data resampling means that it includes variations caused by systematic effects present in the data.

We also compute covariance matrices using 100 QPM mocks [99] for each galactic cap. These mocks take into account cosmic variance, but they struggle to model the correlation function on small scales. However, this is not problematic because these scales are not relevant for this study.

Figure 3 displays the correlation matrices of  $\xi(r)$  for the full eBOSS survey obtained with the mocks and the bootstrap realizations. We note that systematic weighting slightly reduces the amplitude of the off-diagonal elements of the bootstrap correlation matrices on large scales (center compared to left). The mock correlation matrix is noisier because we only have 100 mock catalogues. Figure 4 shows the ratio of bootstrap and mock errors to Poisson errors. We see that bootstrap errors are systematically larger than mock errors, but provide a more accurate determination of uncertainties. The discrepancy between the amplitudes of bootstrap and mock errors arises from the fact that some systematic effects remain in the data after the weighting scheme presented in section 4, and that these effects are not accounted for in the QPM mocks. In the following, we will always display statistical uncertainties obtained from bootstrap realizations.

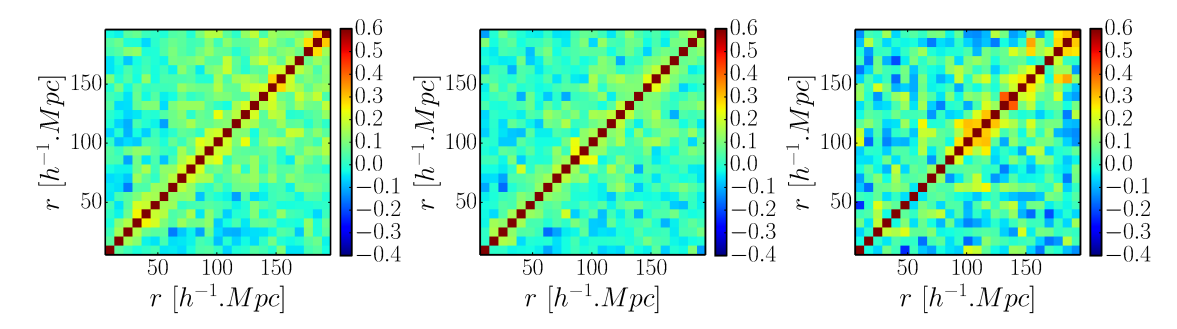


**Figure 3**. Correlation matrices of  $\xi(r)$  computed using bootstrap realizations without systematic weighting (left), with systematic weighting (center), and using QPM mocks (right).

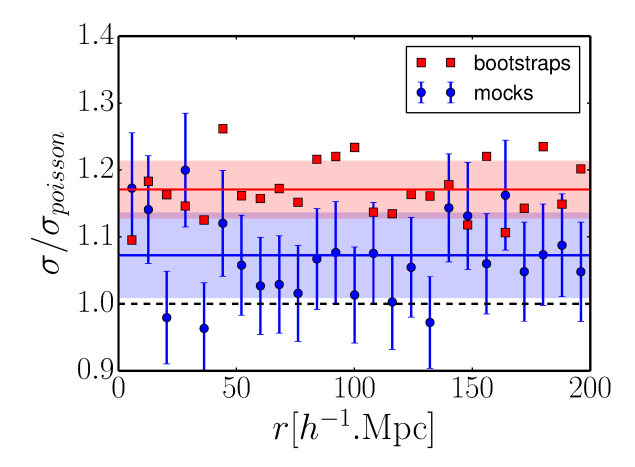


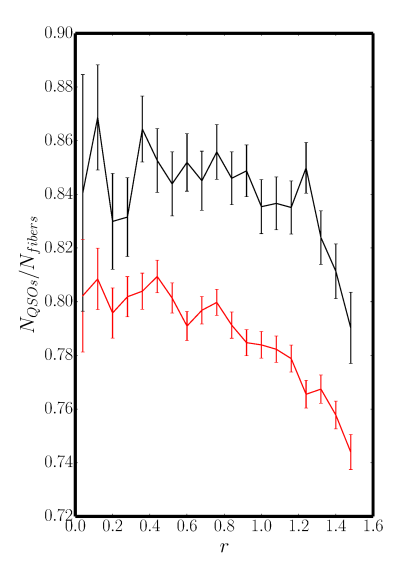
**Figure 4**. Ratio of bootstrap errors to Poisson errors (red squares) and, ratio of mock errors to Poisson errors (blue dots). The lines correspond to the mean value of the ratio, and the bands represent the rms of the dots.

#### 4 Systematic effects

#### 4.1 Inhomogeneities of target identification

The SDSS I-II and BOSS surveys observed a total of 12,759 quasars within our target sample. These "known quasars" were spectroscopically identified by visual inspection [100], whereas newly observed targets are identified automatically by the eBOSS pipeline. The efficiency of target identification is known to be better for the visual inspection than for the pipeline, and such a difference can generate systematic effects. This efficiency also depends on the signal-to-noise ratio, which varies with the position of the fiber in the spectrographs. Fibers with an identifier,  $n_{\rm ID}$ , close to 0, 500 or 1000 are located on the edges of the spectrographs, and their spectra are on average noisier than for other fibers. Since the fiber IDs are also correlated with the position of the fiber in the focal plane, the difference in noise can generate correlations at scales of the order of the plate width.

Figure 5 shows the ratio of the number of identified quasars to the number of fibers,  $N_{\rm QSO}/N_{\rm fibers}$ , versus the distance to the center of the plate, r, and versus the fiber ID,  $N_{\rm ID}$ . The red lines correspond to the newly observed eBOSS targets, identified by the pipeline. The black lines correspond to the targets that have been visually inspected, including all known eBOSS quasars.



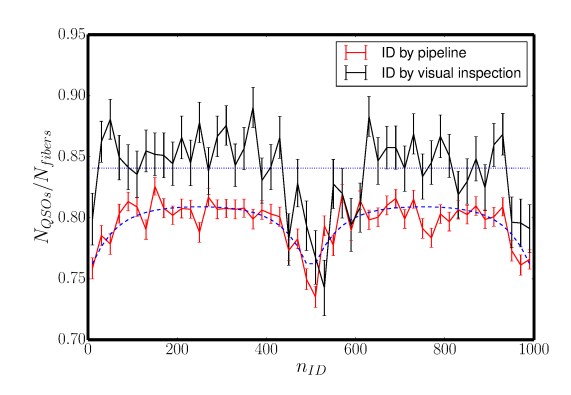


Figure 5. The  $N_{\rm QSO}/N_{\rm fibers}$  ratio with respect to r (left, in radians) and  $n_{\rm ID}$  (right). The black lines correspond to the visually inspected quasar sample, the red lines correspond to the new eBOSS quasar sample, identified by the pipeline. The dashed blue line corresponds to a fit of the function in equation (4.1) on the new eBOSS quasar sample, and the dotted blue lines corresponds to a fit of a constant on the visually inspected quasar sample.

As expected, the ratio  $N_{\rm QSO}/N_{\rm fibers}$  is higher for visually inspected targets than for targets identified with the pipeline, and both ratios present a significant variation with respect to  $n_{\rm ID}$  and r. The dependency with  $n_{\rm ID}$  is well fitted by a hyperbolic cosine with 3 free parameters:

$$\frac{N_{\text{QSO}}}{N_{\text{fibers}}}(n_{\text{ID}}) = -a \cosh\left(\frac{n_{\text{ID}} \mod 500 - 250}{b}\right)^2 + c. \tag{4.1}$$

The resulting fit corresponds to the dashed blue line of figure 5. We correct this effect by weighting eBOSS quasars by the inverse of equation (4.1). Since we do not know the fiber number for all known quasars, we simply weight them with the inverse of the mean value of the ratio, displayed by the blue dotted straight line on figure 5. This takes into account the difference of efficiency of identification between known and new eBOSS quasars. Comparing blue points with magenta dots in figure 7 shows that this unidentification weighting has little effect on  $\xi(r)$ . In addition we also tried a weighting scheme where the hyperbolic cosine dependency for new eBOSS quasars is replaced by the mean value of the ratio, as is done for known quasars. This showed that most of the (small) effect of the unidentification weight comes from the difference of efficiency between the two categories of targets rather than from the dependence of the weight with  $n_{\rm ID}$ . So neglecting the dependence of the weight with  $n_{\rm ID}$  for known quasars is safe.

#### 4.2 Inhomogeneities of quasar target selection

Quasar targets are selected with the XDQSOz algorithm (section 2.2), which aims at providing a homogeneous target selection using the SDSS photometry. The SDSS photometry, however, is not perfectly homogeneous. The mean  $5\sigma$  detection limit for a point source (also called depth) for the SDSS photometry is g = 23.1 and r = 22.7, but it varies with angular position by up to  $\pm 0.8$  magnitude (see histogram on figure 6). Targets are selected up to a

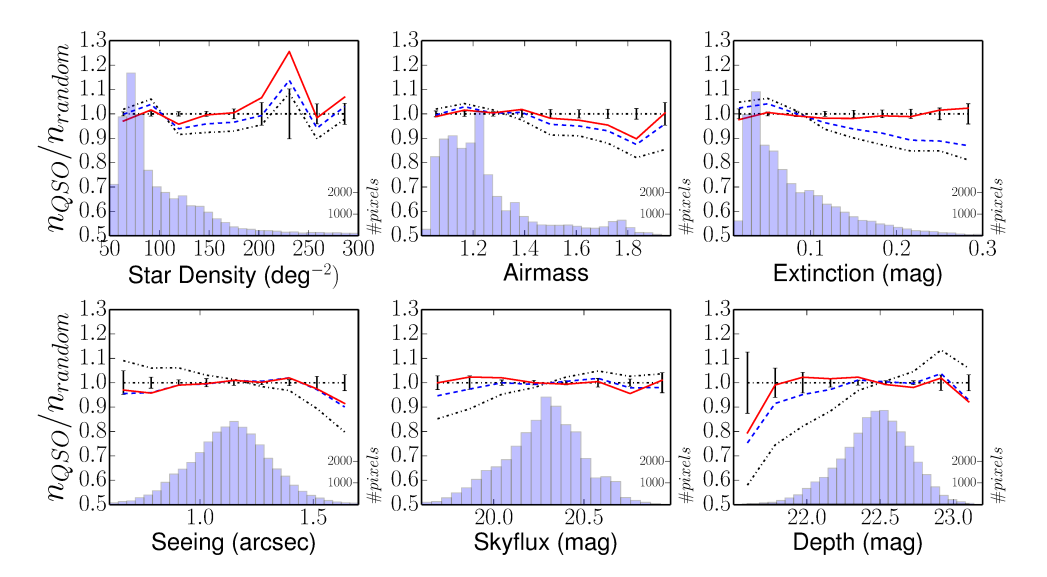


Figure 6. The  $n_{\rm QSO}/n_{\rm randoms}$  ratio versus star density, airmass, Galactic extinction, seeing, sky-flux and depth, for the i-band before any correction (black dotted lines), after correction by the depth (blue dotted lines), and after correction by the depth and the extinction (red full lines). The error bars are computed as the standard error of the mean for  $n_{\rm QSO}/n_{\rm randoms}$  without systematic weighting. For the sake of clarity, the error bars, which are similar before and after weighting, are only displayed once on the  $n_{\rm QSO}/n_{\rm randoms}=1$  line. The histograms display the distribution of pixels for the healpix maps.

given apparent magnitude limit of g = 22.0 or r = 22.0, therefore some faint sources can end up very close to the detection limit. Uncertainties on their relative flux measurements will be significantly higher than for other sources, so the XDQSOz probability of faint sources may go below the selection threshold. Also, observed fluxes of faint sources might be biased by the fluxes of close brighter sources, an effect known as blending.

We study the variation of the observed-quasar density with the depth and its inputs (seeing, airmass, Galactic extinction and sky-flux). We also study the variation with star density, since it can bias the target selection through blending. To do so, we generate Healpix maps with  $N_{\rm side} = 256$  for each of the aforementioned quantities, following the procedure of Ross et al. 2012 [62]. We also create a map for the ratio of the number of observed quasars to the normalized number of random objects: this quantity is proportional to the observed-quasar density corrected for completeness. The black dotted lines on figure 6 show that this ratio varies with all quantities, except star density. This means that we do not observe any bias in the quasar target selection due to blending effects. The dependencies are compatible between the NGC and the SGC, and they do not depend on redshift. We do not observe significant differences by changing the resolution of the Healpix maps to a better one  $(N_{\rm side} = 512)$ . We therefore use the maps with  $N_{\rm side} = 256$ .

We fit a linear function to the dependency with the depth. We weight each quasar with the inverse of the fitted function for the value of the depth in the considered pixel of the map, and recompute the  $n_{\rm QSO}/n_{\rm random}$  ratio. The blue lines in figure 6 show that the dependencies of this ratio with airmass, seeing, sky-flux and depth vanish, and that the dependency with Galactic extinction is reduced, but still significant. The same procedure is applied to the observed-quasar density already corrected for depth to correct for this remaining dependency with Galactic extinction. The final systematic weights for target selection inhomogeneity are obtained by multiplying the depth and Galactic-extinction weights.

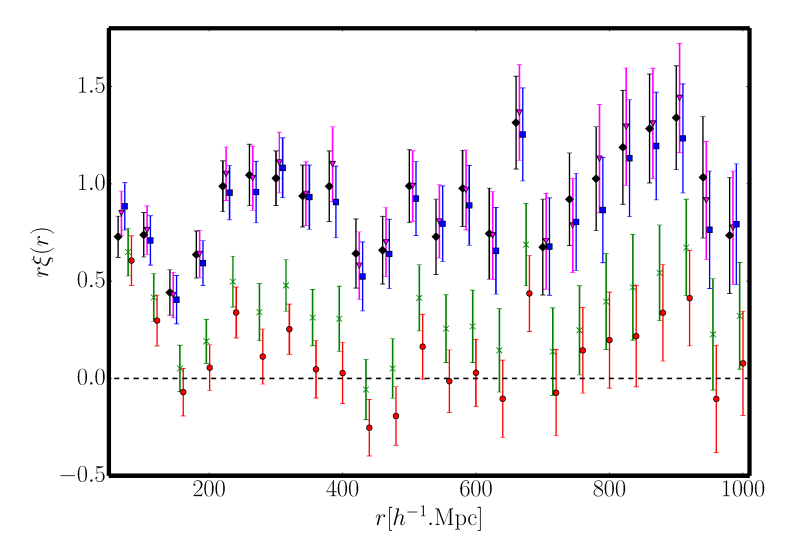


Figure 7. Effects of the different weightings on the quasar correlation function. The black lozenges correspond to  $\xi(r)$  without any weighting, the magenta triangles to  $\xi(r)$  with the collision weights. The blue squares are obtained with the combination of the collision and unidentification weights, the green crosses are obtained with the addition of the depth weights and the red circles are obtained with the addition of the depth and Galactic-extinction weights.

## 4.3 Effect of weightings on $\xi(r)$

Figure 7 shows  $r \cdot \xi(r)$  without any weights, and with the successive addition of collision weights, unidentification weights, depth weights and depth plus Galactic-extinction weights. We quantify the effect of the corrections by computing the cross- $\chi^2$  between  $\xi_N(r)$  and  $\xi_S(r)$ , the correlation functions measured in the NGC and the SGC:

$$\chi_{\rm NS}^2 = \sum_{ij} (\xi_{\rm N}(r_i) - \xi_{\rm S}(r_i)) C_{ij}^{-1} (\xi_{\rm N}(r_j) - \xi_{\rm S}(r_j)), \qquad (4.2)$$

where C is the sum of  $C_N$  et  $C_S$ , the covariance matrices of  $\xi_N(r)$  and  $\xi_S(r)$ . The resulting values are shown in table 1. The main effect clearly arises from weighting with the depth, which strongly reduces the value of  $\chi^2_{NS}$ . The correction for fiber collisions has only a limited impact on larger scales, and is not susceptible to bias the measure of  $b_Q$ . In the following, we will always apply the full weighting scheme to our data sample.

After the application of the full weighting scheme,  $\xi_N(r)$  and  $\xi_S(r)$  are still not fully compatible. This means that some systematic effects are still present, as suggested by the dependency of quasar density with respect to airmass. However, as discussed in Ross et al. [62], applying consecutively angular corrections to the data result in a loss of signal in the correlation function. We therefore choose to restrain the correction of the target selection inhomogeneity to depth and Galactic extinction.

#### 5 Measurement of the quasar bias

In order to measure the quasar bias,  $b_Q$ , we fit the measured  $\xi(r)$  with a flat  $\Lambda$ CDM model, using the same cosmological parameters used for the BOSS twelfth Data Release (namely h=0.676,  $\Omega_m=0.31$ ,  $\Omega_b h^2=0.0220$ ,  $n_s=0.9619$ ). Using these parameters, CAMB [101]

Weighting scheme	$\chi^2_{\rm NS}(24{\rm d.o.f.})$
No weights	161
Collision	154
Collision + Unidentification	128
Collision + Unidentification + Depth	58
Collision + Unidentification + Depth + Galactic extinction	47

**Table 1.** Values of  $\chi^2_{NS}$  (see eq. (4.2)) for different weighting schemes.

provides a non-linear matter power spectrum  $P_{mat}(k)$  for  $10^{-5} < k < 10^2 \,(\text{Mpc/h})^{-1}$ . We account for linear redshift-space-distortions using the Kaiser formula [102]:

$$P_Q(k,\mu) = b_Q^2 (1 + \beta \mu_k^2)^2 P_{mat}(k) , \qquad (5.1)$$

where  $\mu_k$  is the cosine of the angle between k and the line of sight,  $\beta = f/b_Q$ , and  $f \simeq \Omega_m^{0.55}(z)$  is the growth rate of structures. The last step consists in converting  $P_Q(k)$  into  $\xi_Q(r)$  using a Fast Fourier Transform (FFT).

All fits of  $b_Q$  are performed using the MINUIT libraries [103] over the range 10 < r < 85  $h^{-1}{\rm Mpc}$ . MINUIT is a convenient tool used to perform  $\chi^2$  minimization for multi-parameters function, and compute the correlation matrices of the fitted function parameters. The fit, shown on figure 8, exhibits a fair agreement with the  $\Lambda{\rm CDM}$  model ( $\chi^2 = 4.0$  for 7 d.o.f.). For the full eBOSS survey, we measure  $b_Q = 2.45 \pm 0.05$ , for  $\bar{z} = 1.55$ . This result is in agreement with the results obtained by Croom et al. [41] using the 2dF QSO Redshift Survey: their empirical parametrization yields a value  $b_Q(z=1.55)=2.41$ . Croom et al. [41] give the error on the two parameters of their fit but not the correlation. If we neglect the correlation, the error on  $b_Q(z=1.55)$  is 0.30. In any case our measurement is compatible with their parametrization. If we fit their data, we confirm their values of a and b, and find a correlation coefficient  $\rho_{a,b} = -0.90$ . Taking into account this anticorrelation, yields a much lower error on  $b_Q(z=1.55)$  of 0.10. In any case our measurement is compatible with their parametrization.

These results are also compatible with the measurement obtained with the SDSS II quasar sample. The right panel of figure 8 shows that the ratio  $\xi_{QSO}/\xi_{mat} = b_Q^2(1+\frac{2}{3}\beta+\frac{1}{5}\beta^2)$ , where  $\xi_{mat}$  is the matter correlation function, remains nearly constant with r. This means that our measurement of  $b_Q$  is not sensitive to the range of the fit.

We cut our sample in 4 redshift slices, and measure  $b_Q$  in each subsample: the results are displayed on figure 9, alongside results from the BOSS quasar sample from Laurent et al. [69]. The numerical values are presented in table 2. We combine the measurements of  $b_Q$  from the eBOSS and BOSS samples, and fit  $b_Q(z)$  using MINUIT. In order to avoid a large anti-correlation between the fit parameters obtained with Croom parametrization, we use an equivalent parametrization defined such as to yield non correlated parameters:

$$b_Q(z) = \alpha[(1+z)^2 - 6.565)] + \beta \tag{5.2}$$

with

$$\alpha = 0.278 \pm 0.018, \quad \beta = 2.393 \pm 0.042, \quad \rho_{\alpha,\beta} = 0,$$
 (5.3)

where  $\rho_{\alpha,\beta}$  is the correlation coefficient between the parameters  $\alpha$  and  $\beta$ . This is equivalent to  $a=0.278\pm0.018,\,b=0.57\pm0.13$  and  $\rho_{a,b}=-0.94$ , consistent with Croom et al.

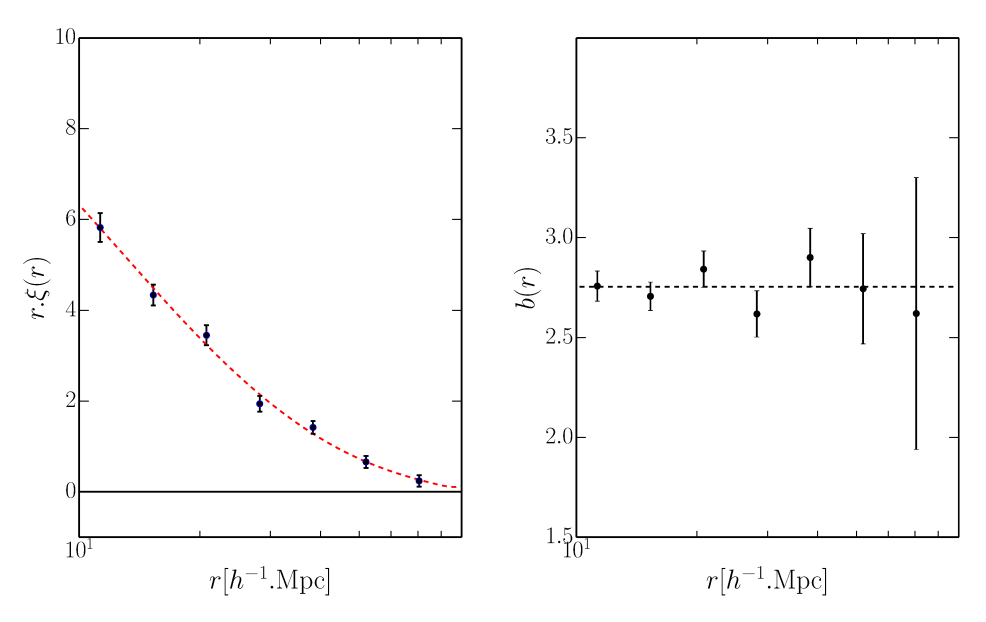


Figure 8. Left:  $\xi(r)$  for the eBOSS survey (black dots). The red dashed curve is a  $\Lambda$ CDM fit to the data. Right: measured quasar effective bias ( $\xi_{QSO}/\xi_{mat,CAMB}$ ) as a function of the separation r. The bias is compatible with a constant, even on larger scales due to systematic weighting.

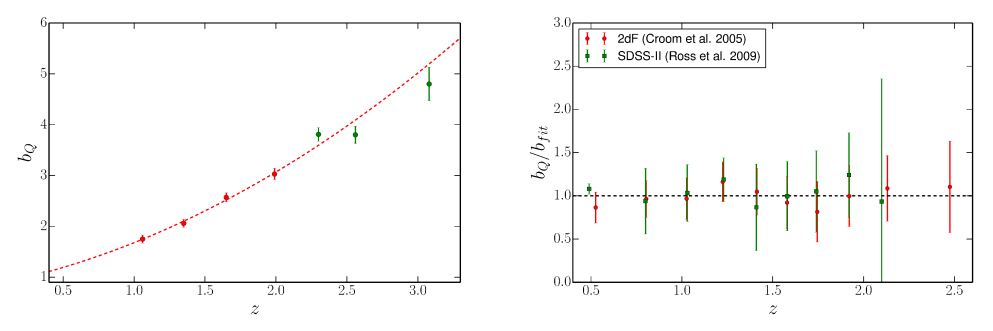


Figure 9. Left: measured quasar bias as a function of redshift. The red dots correspond to this analysis (eBOSS data) and the green dots correspond to the bias measured with the BOSS sample, in the range 2.2 < z < 3.5 [69]. The red dotted line is the fit  $b_Q(z) = a(1+z)^2 + b$ . Right: ratio of quasar bias measured by previous surveys to the value of the function fitted on the results of the eBOSS and BOSS samples. The red dots correspond to the 2dF sample, the blue squares to the SDSS-II quasar sample.

The right panel of figure 9 displays the ratio of the quasar bias measured by the 2dF and the SDSS-II surveys to the value of our fitted function. Our results appear again to be compatible with former analyses of quasar clustering. We also stress that, with only one fifth of its final statistic, the eBOSS quasar sample already provides the most accurate measurement of the quasar bias in the redshift range 0.9 < z < 2.2.

## 6 The halo mass and the duty cycle of eBOSS quasars

We now discuss possible implications of our measurements of the clustering of  $\sim 70,000$  eBOSS quasars for the host dark matter haloes of quasars at  $1 \lesssim z \lesssim 2$ . We quantify the

$z_{ m min}$	$z_{ m max}$	$z_{ m eff}$	$N_{ m QSO}$	$b_Q$	$\chi^2 \ (7 \ d.o.f.)$
0.9	1.2	1.06	$13,\!594$	$1.75 \pm 0.08$	9.9
1.2	1.5	1.35	17,696	$2.06 \pm 0.08$	1.7
1.5	1.8	1.65	17,907	$2.57 \pm 0.09$	2.1
1.8	2.2	1.99	$19,\!575$	$3.03 \pm 0.11$	8.5
0.9	2.2	1.55	68,772	$2.43 \pm 0.05$	4.5

**Table 2**. Fit of bias over  $10 < r < 85 \ h^{-1}{\rm Mpc}$  in various redshift bins.

activity of eBOSS quasars by calculating their duty cycle, through which the halo mass of a population of quasars can be linked to their luminosity.

## 6.1 Characteristic Halo Mass

Quasars are biased tracers of underlying dark matter [104] and the fact that more massive haloes have higher clustering bias [105, 106], has been used as the basis for constraining the mass of the dark matter haloes that host quasars [49, 104, 107–109]. Here, we follow a similar approach to Eftekharzadeh et al. [49], who constrained the dark matter halo mass and duty cycle of  $\sim 75,000$  quasars at  $z \sim 2.5$  in the final release of the BOSS survey.

We adopt parameters such as to get a  $\Delta=200$  matter overdensity in the formalism of Tinker et al. [106] in order to calculate the minimum halo mass,  $M_{h, \min}$ , and the characteristic halo mass,  $\bar{M}_h$ , of our quasars. We apply this approach to quasars in our main sample, and in each of our four redshift subsamples (detailed in table 3). In this formalism,  $\bar{M}_h$  is the characteristic halo mass that corresponds to our measured clustering bias, i.e.  $b(\bar{M}_h) = b_Q$ , and  $M_{h, \min}$  is the minimum halo mass that bounds the range of haloes that correspond to the observed clustering bias, i.e.  $b(M>M_{h, \min})=b_Q$ , with

$$b(M > M_{h,\min}) \equiv \frac{\int_{M_{h,\min}}^{\infty} \frac{\mathrm{d}n}{\mathrm{d}M} b(M) \mathrm{d}M}{\int_{M_{h,\min}}^{\infty} \frac{\mathrm{d}n}{\mathrm{d}M} \mathrm{d}M}, \tag{6.1}$$

where the halo masses above  $M_{h,\text{min}}$  are weighted by the halo abundance  $\mathrm{d}n/\mathrm{d}M$  in the halo mass function as determined by Tinker et al. [110]. To calculate  $M_{h,\mathrm{min}}$ , using a Monte Carlo approach, we run a large range of possible models through the fitting procedure and determine the best fit and 68% range of errors to derive the confidence limits.

The assumption of a lower limit  $M_{h,\rm min}$  in eq. 6.1, suggests that haloes with  $M < M_{h,\rm min}$  can only host quasars that are less luminous than the least luminous quasar in our sample. This interpretation can be tested for consistency by checking whether quasar clustering is luminosity-dependent. For example, Eftekharzadeh et al. [49] found that the assumption of a scatter-less monotonic relation between halo mass and quasar luminosity failed to describe the observed lack of luminosity dependence for the clustering of BOSS quasars at  $z \sim 2.4$ . How quasar clustering varies with luminosity appears to be a subtle effect. Categorically detecting whether different luminosity quasars are hosted by different mass haloes will therefore require very precise measurements of quasar clustering. Constraining any luminosity dependence to quasar clustering is a topic where eBOSS could make gains, given its expected unprecedentedly large sample of homogeneously selected quasars.

Prior to eBOSS, the most extensive wide-area spectroscopic quasar surveys at  $z \sim 1.5$  that were used for clustering analyses, were the 2dFQSO redshift survey (2QZ; [111, 112]) and

the SDSS-DR5 quasar survey (DRQ5; [113, 114]). Restricting to uniformly selected quasars over the redshift range 0.9 < z < 2.2, these surveys provided catalogs of  $\sim 20,000$ –25,000 quasars with which to conduct clustering analyses. Projecting from SEQUELS, eBOSS is expected to spectroscopically confirm  $\sim 70$  quasars per deg<sup>2</sup> down to a limiting magnitude of g < 22 over  $\sim 7,500\,\mathrm{deg^2}$ , for a total sample of more than 500,000 uniformly selected quasars in the redshift range 0.9 < z < 2.2 [83]. The average magnitude of eBOSS quasars is  $\sim 2.5$  times fainter than that of previous SDSS clustering samples, while covering a similar redshift range. Essentially, therefore, eBOSS will extend quasar clustering measurements by about a factor of 10 in luminosity. This unprecedented expansion of the dynamical range and number density of quasar samples will allow eBOSS to provide the highest statistical power yet to disentangle the luminosity and redshift dependences of quasar clustering.

Figure 10 shows  $M_{h, \rm min}$  and  $\bar{M}_h$  for our full (NGC+SGC) sample of 68,772 quasars at  $z\sim 1.5$ , as well as for our four redshift subsamples at z=1.06,~1.35,~1.65,~ and 1.99. In addition, the 4th and 5th columns of table 4 list the  $\bar{M}_h$  and  $M_{h, \rm min}$  we derive for our four redshift subsamples as well as for our main sample. The errors on  $\bar{M}_h$  and  $M_{h, \rm min}$  are calculated from the confidence intervals for the quasar biases that we derive from our clustering measurements. These confidence intervals are projected through eq. 6.1 at the mean redshift of each sample, using the Tinker et al. [110] halo mass function and the appropriate values of  $M_{h, \rm min}$ , in order to derive a corresponding confidence interval in halo mass.

To illustrate how  $M_{h,\min}$  and  $\bar{M}_h$  change over the redshift range that is covered by both BOSS (z > 2.2) and eBOSS (z < 2.2), figure 10 displays the measurements made by Eftekharzadeh et al. [49] for BOSS quasars using the same formalism that we use here for eBOSS quasars. Figure 10 also includes the same quantities estimated using the quasar clustering measurements from Shen et al. [45] at  $z \sim 3.1$  and  $z \sim 4.0$  and Font-Ribera et al. [115] at  $z \sim 2.4$ . Note that the agreement between Font-Ribera et al. [115] and Eftekharzadeh et al. [49] is not particularly surprising, as both measurements are made using BOSS quasars. However, the reason for the extreme differences in halo mass measured by Shen et al. [45], as compared to lower-redshift studies, remains debatable. Shen et al. [45] studied the clustering of a sample of  $\sim 4000$  highly luminous quasars with a density of  $\sim 1\,\mathrm{deg}^{-2}$  and measured quasar biases approaching  $b_{\rm Q} \sim 16$  at z > 4. It is possible that there is a sharp change in the host halo mass of quasars that lie beyond the luminosity and redshift range of BOSS models in which quasars are triggered by major mergers of gas-rich galaxies [116] do allow for evolutionary scenarios in which the clustering of luminous quasars simply tracks the growth of the most massive haloes at z > 3. Indeed, the duty cycle of  $f_{\rm duty} \sim 1$  measured by Shen et al. [45] for quasars at z > 3 implies that all rare supermassive haloes (>  $10^{13} M_{\odot}$ ) host active black holes.

Previous authors [112] found convincing evidence that the bias of z < 2.5 quasars, at magnitudes of about g < 21, increases with redshift from  $z \sim 0.5$  to  $z \sim 2.5$ . This implies that the mass of the haloes hosting quasars remains fairly constant at z < 2.5, because a higher bias can offset the fact that the characteristic mass of the average halo must dwindle at higher redshift (as structure has had less time to grow). By extension, if the bias of quasars were to remain constant at higher and higher redshift, this would imply that the characteristic mass of the haloes hosting quasars was decreasing with redshift. Essentially this dwindling host halo mass was what was found by Eftekharzadeh et al. [49] for BOSS quasars at z > 2.5, as is shown in figure 10. Contrary to the flat  $b_Q(z)$ , or dwindling host halo mass, measured for BOSS quasars at z > 2.5, the biases we measure for eBOSS quasars increase with redshift, implying that the characteristic host halo mass of eBOSS quasars is

roughly constant (again as shown in figure 10). This is in excellent agreement with the results of Croom et al. [112], who found a non-evolving halo mass of  $M=(3.0\pm1.6)\times10^{12}\,h^{-1}M_{\odot}$  over 0.5< z<2.5 for a smaller sample of quasars that were slightly more luminous than those in our sample.

## 6.2 Duty cycle

The length of duration of the quasar phase (the so-called "duty cycle") has been defined in multiple slightly different ways in the literature. Here, we take the definition of the duty cycle as the ratio of the number density of haloes that host black holes that are "on" (and thus observed as luminous quasars) to the full number of haloes that could host quasars within the luminosity range of our sample. As in Eftekharzadeh et al. [49], we compare the cumulative luminosity function of quasars over a range of luminosities to the cumulative space density of haloes over the corresponding range of host halo masses [104, 108]

$$f_{\text{duty}} = \frac{\int_{L_{\text{min}}}^{L_{\text{max}}} \Phi(L) dL}{\int_{M_{\text{h,min}}}^{\infty} \frac{dn}{dM} dM},$$
(6.2)

where the value of  $M_{h,\rm min}$  is set by the measured quasar bias (as in eq. 6.1),  ${\rm d}n/{\rm d}M$  is, again, taken from Tinker et al. [110], and  $\Phi(L)$  is the quasar luminosity function. Note that we integrate our halo masses over the entire mass range from  $M_{h,\rm min}$  to infinity.<sup>2</sup> Effectively, this reflects the extremely weak relationship between quasar clustering and quasar luminosity, by allowing the quasars in our samples to be hosted by a limitless range of halo masses above  $M_{h,\rm min}$ . We adopt a recent quasar luminosity function from Palanque-Delabrouille et al. [84] that was derived using quasars in our redshift and luminosity ranges of interest. We use this luminosity function to calculate the space density of quasars in our samples (see the 3rd column in table 4). Quasars targeted as part of eBOSS do not all receive a fiber for follow-up spectroscopy. Further, eBOSS is not complete to all quasars in the Universe. Hence, the observed number density of quasars listed in table 3 should be lower than the expected total space density of 0.9 < z < 2.2 quasars at the flux limit of eBOSS, even if the Palanque-Delabrouille et al. [84] luminosity function is perfectly accurate.

We display our calculated  $f_{\rm duty}$  values as a function of redshift in figure 11 and list the corresponding measurements in table 4. Motivating by the fact that the error on the bias dominates any errors on the luminosity function, we estimate errors on  $f_{\rm duty}$  by drawing sample values of the quasar bias from a Gaussian corresponding to the 68% confidence interval around our measured  $\pm 1\sigma$  errors on  $b_{\rm Q}$ . It is however worth emphasising that the resulting errors were not forced to follow a Gaussian distribution but a 68% Gaussian range on the variables were chosen to go into the fitting analysis and take any form after passing naturally through the model in a Monte-Carlo fashion. We then calculate  $f_{\rm duty}$  for each sampled  $b_{\rm Q}$  using eq. 6.1 and eq. 6.2, and hence derive the implied  $\pm 1\sigma$  errors on  $f_{\rm duty}$ . Figure 11 compares our results to the similarly calculated  $f_{\rm duty}(z)$  of BOSS quasars at z > 2.2from Eftekharzadeh et al. [49].

Under the assumption that there is effectively no link between the luminosity and clustering of quasars (i.e. the assumption that we used to derive  $f_{\rm duty}$ ), we can ignore the different luminosity ranges probed by BOSS and eBOSS and directly compare the host halo masses and duty cycles of BOSS and eBOSS quasars. The almost flat  $\bar{M}_h(z)$  up until  $z \sim 1.8$  depicted in figure 10, implies that quasars reside in haloes of similar mass at  $z \lesssim 2$ . Above

<sup>&</sup>lt;sup>2</sup>The infinity in this equation has a numerical equivalent of  $\sim 10^{15} \, h^{-1} M_{\odot}$ .

 $z\sim2$ , the characteristic mass of the haloes that host quasars appears to plummet, by almost a dex by  $z\sim3$ . Further, as listed in table 4, the measured duty cycle for eBOSS quasars at  $\bar{z}\sim1.5$  is more than four times longer than for BOSS quasars at  $\bar{z}\sim2.5$ . It has long been known that the quasar population peaks in space density around redshift 2–3 [117]. We can interpret this peak as a physical manifestation

of a combination of the quasar duty cycle and the characteristic masses of quasar-hosting haloes. As more massive haloes are rarer,  $z\sim 2$ –3 is a sweet-spot where duty cycles are large compared to host halo rarity. Below  $z\sim 2$  quasar-hosting haloes are equally as rare as they are at  $z\sim 2$  (because the characteristic halo mass is unchanging) but the increasingly small duty cycle at lower redshifts implies that fewer of these haloes host active quasars. in contrast, at  $z\sim 2$ –3, the characteristic mass of quasar-hosting haloes drops, which implies that quasar-hosting haloes are more common. This, however, is offset somewhat by a rapid reduction in the duty cycle, which implies that at higher redshifts in the range  $z\sim 2$ –3 fewer and fewer quasars are "on" in these increasingly more numerous haloes.

On the other hand, our assumption that there is absolutely no correlation between quasar luminosity and host halo mass may break down under further scrutiny. More sophisticated models that add scatter to the halo mass-luminosity relation [118] would then be needed to fully understand the interplay between quasars and large-scale structure. The characteristic mass of the haloes that host quasars is an average across the halo mass function (dn/dM), so the fact that the characteristic mass stays relatively constant between  $z\sim 2$ and  $z \sim 1$  could simply mean that the most massive haloes dominate this average. A plausible scenario might be that less luminous quasars inhabit a wide range of halo masses but more luminous quasars only reside in the most massive haloes. At  $z \sim 1$ , where we sample far down the quasar luminosity function, we might then expect to see a wide range of halo masses, but the clustering signal would still be dominated by the most massive haloes. At  $z \sim 2$ , where our magnitude-limited sample would shift to more luminous quasars, we would increasingly sample just higher-mass haloes. In either case, at  $z\sim 1$  or at  $z\sim 2$  our clustering signal would only reflect the clustering of high mass haloes. It is straightforward to interpret our measurements under this alternative scenario. For example, table 4 shows that quasars in our first redshift subsample at 0.9 < z < 1.2 are the least luminous population, on average, among our four redshift subsamples, and that there are also fewer of them. These 0.9 < z < 1.2 quasars have an  $M_{h,\text{min}}$  that is somewhat smaller than the 2–3× more luminous population at 1.5 < z < 1.8, but have an  $\bar{M}_h$  that is consistent. This could be interpreted to be indicative of the less-luminous-than average 0.9 < z < 1.2 quasars occupying the widest range of halo masses in eBOSS but, also being less numerous, still having a clustering signal that is dominated by the most massive haloes.

Our sample of quasars is of insufficient size to detect any luminosity dependence to quasar clustering. But, as was mentioned earlier in this section, a detailed study of the luminosity dependence of quasar clustering using the final eBOSS sample of  $\sim 500,000$  quasars remains an important and highly anticipated objective of the eBOSS survey. In addition, the quasars sampled by eBOSS overlap the Luminous Red Galaxy and Emission Line Galaxy populations sampled by eBOSS around  $0.7 \lesssim z \lesssim 1.0$ . This will provide a chance to cross correlate quasars with more-numerous galaxies (as in, e.g., [119, 120]) to try to study the luminosity dependence of quasar clustering in narrow redshift bins near  $z \sim 0.8$ .

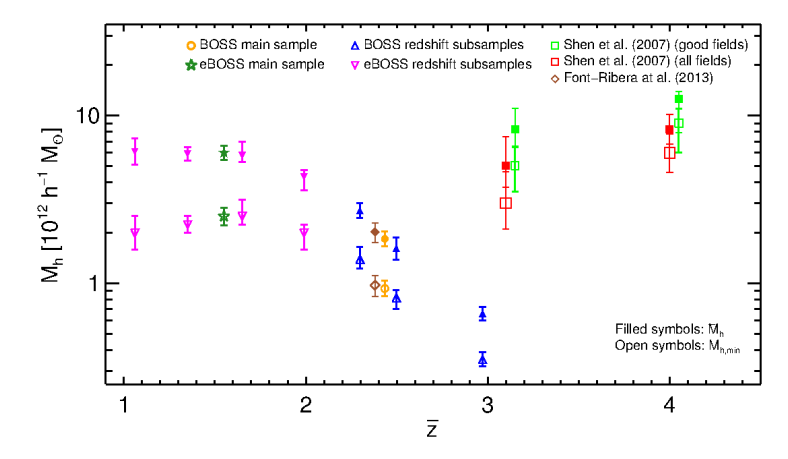


Figure 10. The evolution of the minimum and characteristic halo mass (see also eq. 6.1 and table 4) for our full sample (green stars) and four redshift subsamples (pink inverted triangles). Other points indicate the results for BOSS from Eftekharzadeh et al. [49] for their main sample (orange circle) and three redshift subsamples (blue triangles), from Shen et al [45] (the "good fields" points have been offset slightly for visual clarity), and from Font-Ribera et al. [115]. Results from previous works are based on their reported values of quasar bias, recalibrated to our chosen cosmology.

$\Delta z$	$\Delta M_i$	$N_{ m qso}$	n
			$(10^{-6} h^{-1} \mathrm{Mpc})^{-3}$
$0.9 \le z < 1.2$	$-22.05 \le M_i \le -26.77$	13594	$13.94 \pm 0.27$
$1.2 \le z < 1.5$	$-22.62 \le M_i \le -27.33$	17696	$15.20\pm0.26$
$1.5 \le z < 1.8$	$-22.97 \le M_i \le -27.81$	17907	$13.98 \pm 0.27$
$1.8 \le z < 2.2$	$-23.49 \le M_i \le -28.22$	19575	$10.87 \pm 0.30$
$0.9 \le z \le 2.2$	$-22.82 \le M_i \le -27.67$	68772	$13.17 \pm 0.28$

**Table 3**. The redshift limits, absolute *i*-magnitude range, total number of quasars (NGC+SGC) and space density in comoving coordinates for quasars in our main sample (final row) and redshift subsamples.

## 7 Conclusion

The first year of observation of the eBOSS survey provides 68,772 homogeneously selected quasars in the redshift range 0.9 < z < 2.2, which represents the largest quasar sample ever obtained in this redshift range. We use this quasar sample to measure the quasar correlation function  $\xi(r)$ . We investigate various sources of systematic effects that might impact the measurement of  $\xi(r)$ , and find that the main contribution arises from inhomogeneities in the quasar target selection. We provide a weighting scheme that mitigates the important systematic effects, and we show that the resulting correlation function is much closer to zero on large scales

The measured correlation function is in agreement with a linear  $\Lambda$ -CDM model in the range  $10 < r < 85 \ h^{-1}$ Mpc. We measure the quasar bias of our sample to be  $b_Q = 2.45 \pm 0.05$ , at  $\bar{z} = 1.55$ . Splitting our sample into four redshift slices provides the evolution of  $b_Q$  with redshift, and confirms that  $b_Q$  increases with z in the studied redshift range. These results are compatible with previous findings by the 2dF and SDSS-II surveys. It is also remarkable

$\Delta z$	$\Delta L$	$\Phi(L_{\min} < L < L_{\max})$	$M_{h,\mathrm{min}}$	$\overline{M}_{ m h}$	$f_{ m duty}$
	$(10^{46}\mathrm{erg}\mathrm{s}^{-1})$	$(10^{-6}  h^{-1} \mathrm{Mpc})^{-3}$	$(10^{12}h^{-1}M_{\odot})$	$(10^{12}h^{-1}M_{\odot})$	
$0.9 \le z < 1.2$	$0.04 \le L \le 2.96$	$16.96^{+1.54}_{-1.78}$	$1.99^{+0.52}_{-0.41}$	$6.10^{+1.20}_{-1.00}$	$0.0091 \pm 0.0027$
$1.2 \le z < 1.5$	$0.06 \leq L \leq 4.94$	$23.69^{+2.46}_{-2.19}$	$2.24^{+0.27}_{-0.24}$	$5.91^{+0.56}_{-0.51}$	$0.0183 \pm 0.0028$
$1.5 \le z < 1.8$	$0.09 \leq L \leq 7.68$	$29.37_{-2.99}^{+2.91}$	$2.51^{+0.65}_{-0.27}$	$5.80^{+1.20}_{-0.51}$	$0.0355 \pm 0.0133$
$1.8 \le z \le 2.2$	$0.14 \leq L \leq 11.23$	$32.89_{-3.56}^{+3.10}$	$1.99^{+0.24}_{-0.41}$	$4.33_{-0.74}^{+0.42}$	$0.0422 \pm 0.0077$
$0.9 \le z \le 2.2$	$0.04 \le L \le 11.23$	$26.82^{+2.11}_{-2.42}$	$2.51^{+0.31}_{-0.27}$	$6.01^{+0.58}_{-0.58}$	$0.0292 \pm 0.0048$

Table 4. The first two columns display the redshift limits and luminosity range for our main sample (final row) and redshift subsamples. The 3rd column lists the space density of quasars in the given redshift and luminosity ranges, calculated using the combination of the Pure Luminosity Evolution (PLE) and the Luminosity and Density Evolution (LEDE) models for the luminosity function (PLE+LEDE) from Palanque-Delabrouille et al. [84]. The 4th and 5th columns display the minimum and the characteristic halo mass calculated at the average redshift of the sample (see eq. 6.1). The 6th column lists the duty cycle, which is derived from  $M_{h,\min}$  and  $\Phi$  (see eq. 6.2).  $f_{\text{duty}}$  is expressed as a fraction of the Hubble time (9.785  $h^{-1}$  Gyr in our adopted cosmology).

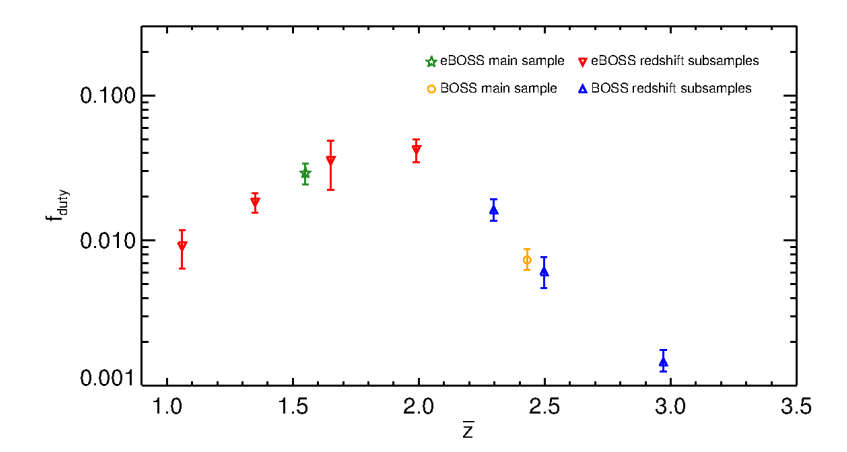


Figure 11. The evolution of the duty cycle for our main sample (green star) and four redshift subsamples (red inverted triangles) calculated using eq. 6.2. See table 4 for the  $f_{\rm duty}$  values and table 3 for a summary of each sample's physical properties. Triangles depict values of  $f_{\rm duty}$  for BOSS quasars from Eftekharzadeh et al. [49] for their main sample (orange circle) and their three redshift subsamples (blue triangles).

that, with only one fifth of the final sample, the eBOSS survey already provides the most accurate measurement of  $b_Q(z)$  in the range 0.9 < z < 2.2.

Adopting Tinker et al. [106]'s formalism for the dark matter distribution and halo mass function, we calculate the minimum halo mass,  $M_{h,\text{min}}$ , and the characteristic halo mass,  $\bar{M}_h$ , of our quasar sample. We use a recent luminosity function that was derived using quasars in our redshift and luminosity ranges of interest [84] to measure the duty cycle of eBOSS quasars at  $z \sim 1.5$  and for subsamples of these quasars in four slices of redshift over 0.9 < z < 2.2 to investigate the redshift evolution of  $M_{h,\text{min}}$ ,  $\bar{M}_h$ , and  $f_{\text{duty}}$ . We conduct our  $M_{h,\text{min}}$ ,  $\bar{M}_h$ , and  $f_{\text{duty}}$  calculations under the assumption that there is weak to no connection between

quasar clustering and quasar luminosity. This assumption allowed us to compare the same calculations for BOSS quasars at z > 2.2 to our measurements for much fainter quasars at z < 2.2.

We find that the characteristic mass of haloes hosting quasars remains relatively constant at z < 2.2. This finding is in agreement with the non-evolving halo mass of quasars over 0.5 < z < 2.2 found by Croom et al. [112]. Our result is also in accord with the dwindling halo mass found for BOSS quasars at z > 2.2 by Eftekharzadeh et al. [49] as the structures have more time to grow at higher redshifts than at z < 2 (see figure 10). We find the duty cycle of eBOSS quasars at  $\bar{z} \sim 1.5$  to be more than four times longer than that of BOSS quasars at  $\bar{z} \sim 2.5$ . Combining the duty cycles of BOSS and eBOSS quasars in figure 11, we interpret the observed peak at the quasar duty cycle around  $z \sim 2$  as a physical manifestation of having fewer quasars that are "on" at  $z \sim 2-3$ . The average luminosity of eBOSS quasars at 0.9 < z < 1.2 in our sample is 2-3 times less than quasars at 1.5 < z < 1.8 and they appear to occupy a wider range of halo masses with smaller  $M_{h,\min}$  compared to quasars at 1.5 < z < 1.8 (see table 4). Nevertheless, the clustering signal for both sets of quasars is dominated by the rare most massive halos in their occupied range of halo masses. The size of our current sample of quasars in the first year of eBOSS is insufficient to detect any luminosity dependence to quasar clustering. Whether quasar clustering is luminosity-dependent will be further investigated with the final sample of  $\sim 500,000$  eBOSS quasars.

## Acknowledgments

Funding for the Sloan Digital Sky Survey IV has been provided by the Alfred P. Sloan Foundation, the U.S. Department of Energy Office of Science, and the Participating Institutions. SDSS acknowledges support and resources from the Center for High-Performance Computing at the University of Utah. The SDSS web site is www.sdss.org.

SDSS is managed by the Astrophysical Research Consortium for the Participating Institutions of the SDSS Collaboration including the Brazilian Participation Group, the Carnegie Institution for Science, Carnegie Mellon University, the Chilean Participation Group, the French Participation Group, Harvard-Smithsonian Center for Astrophysics, Instituto de Astrofísica de Canarias, The Johns Hopkins University, Kavli Institute for the Physics and Mathematics of the Universe (IPMU) / University of Tokyo, Lawrence Berkeley National Laboratory, Leibniz Institut für Astrophysik Potsdam (AIP), Max-Planck-Institut für Astronomie (MPIA Heidelberg), Max-Planck-Institut für Astrophysik (MPA Garching), Max-Planck-Institut für Extraterrestrische Physik (MPE), National Astronomical Observatories of China, New Mexico State University, New York University, University of Notre Dame, Observatório Nacional / MCTI, The Ohio State University, Pennsylvania State University, Shanghai Astronomical Observatory, United Kingdom Participation Group, Universidad Nacional Autónoma de México, University of Arizona, University of Colorado Boulder, University of Oxford, University of Portsmouth, University of Utah, University of Virginia, University of Washington, University of Wisconsin, Vanderbilt University, and Yale University.

SE and ADM were partially supported by NSF grants 1515404 and 1616168 and NASA grant NNX16AN48G. ADM was also partially supported by the Director, Office of Science, Office of High Energy Physics of the U.S. Department of Energy under Contract No. DE-AC02-05CH1123.

#### References

- [1] COBE collaboration, G.F. Smoot et al., Structure in the COBE differential microwave radiometer first year maps, Astrophys. J. 396 (1992) L1 [INSPIRE].
- [2] C.L. Bennett et al., Four year COBE DMR cosmic microwave background observations: maps and basic results, Astrophys. J. 464 (1996) L1 [astro-ph/9601067] [INSPIRE].
- [3] WMAP collaboration, C.L. Bennett et al., First year Wilkinson Microwave Anisotropy Probe (WMAP) observations: preliminary maps and basic results, Astrophys. J. Suppl. 148 (2003) 1 [astro-ph/0302207] [INSPIRE].
- [4] WMAP collaboration, E. Komatsu et al., Five-year Wilkinson Microwave Anisotropy Probe (WMAP) observations: cosmological interpretation, Astrophys. J. Suppl. 180 (2009) 330 [arXiv:0803.0547] [INSPIRE].
- [5] Planck collaboration, P.A.R. Ade et al., *Planck 2013 results. XVI. Cosmological parameters*, *Astron. Astrophys.* **571** (2014) A16 [arXiv:1303.5076] [INSPIRE].
- [6] Planck collaboration, P.A.R. Ade et al., *Planck 2015 results. XIII. Cosmological parameters*, *Astron. Astrophys.* **594** (2016) A13 [arXiv:1502.01589] [INSPIRE].
- [7] M. Chevallier and D. Polarski, Accelerating universes with scaling dark matter, Int. J. Mod. Phys. **D** 10 (2001) 213 [gr-qc/0009008] [INSPIRE].
- [8] E.V. Linder, Cosmic growth history and expansion history, Phys. Rev. D 72 (2005) 043529 [astro-ph/0507263] [INSPIRE].
- [9] D.H. Weinberg, M.J. Mortonson, D.J. Eisenstein, C. Hirata, A.G. Riess and E. Rozo, Observational probes of cosmic acceleration, Phys. Rept. 530 (2013) 87 [arXiv:1201.2434] [INSPIRE].
- [10] M.J. Drinkwater et al., The WiggleZ dark energy survey: survey design and first data release, Mon. Not. Roy. Astron. Soc. 401 (2010) 1429 [arXiv:0911.4246] [INSPIRE].
- [11] J.J. Adams et al., The HETDEX pilot survey. I. Survey design, performance and catalog of emission-line galaxies, Astrophys. J. Suppl. 192 (2011) 5 [arXiv:1011.0426] [INSPIRE].
- [12] BOSS collaboration, K.S. Dawson et al., The Baryon Oscillation Spectroscopic Survey of SDSS-III, Astron. J. 145 (2013) 10 [arXiv:1208.0022] [INSPIRE].
- [13] DESI collaboration, M. Levi et al., *The DESI experiment, a whitepaper for Snowmass 2013*, arXiv:1308.0847 [INSPIRE].
- [14] K.S. Dawson et al., The SDSS-IV extended Baryon Oscillation Spectroscopic Survey: overview and early data, Astron. J. 151 (2016) 44 [arXiv:1508.04473] [INSPIRE].
- [15] J. Huchra, M. Davis, D. Latham and J. Tonry, A survey of galaxy redshifts. IV The data, Astrophys. J. Suppl. 52 (1983) 89.
- [16] S.A. Shectman et al., The Las Campanas redshift survey, Astrophys. J. 470 (1996) 172 [astro-ph/9604167] [INSPIRE].
- [17] W. Saunders et al., The PSCz catalogue, Mon. Not. Roy. Astron. Soc. 317 (2000) 55 [astro-ph/0001117] [INSPIRE].
- [18] 2DFGRS collaboration, M. Colless et al., The 2dF galaxy redshift survey: spectra and redshifts, Mon. Not. Roy. Astron. Soc. 328 (2001) 1039 [astro-ph/0106498] [INSPIRE].
- [19] J.A. Newman et al., The DEEP2 galaxy redshift survey: design, observations, data reduction and redshifts, Astrophys. J. Suppl. 208 (2013) 5 [arXiv:1203.3192] [INSPIRE].
- [20] SDSS collaboration, D.G. York et al., The Sloan Digital Sky Survey: technical summary, Astron. J. 120 (2000) 1579 [astro-ph/0006396] [INSPIRE].

- [21] SDSS collaboration, M.A. Strauss et al., Spectroscopic target selection in the Sloan Digital Sky Survey: the main galaxy sample, Astron. J. 124 (2002) 1810 [astro-ph/0206225] [INSPIRE].
- [22] SDSS collaboration, D.J. Eisenstein et al., Spectroscopic target selection for the Sloan Digital Sky Survey: the luminous red galaxy sample, Astron. J. 122 (2001) 2267 [astro-ph/0108153] [INSPIRE].
- [23] 2DFGRS TEAM collaboration, W.J. Percival et al., Parameter constraints for flat cosmologies from CMB and 2dFGRS power spectra, Mon. Not. Roy. Astron. Soc. **337** (2002) 1068 [astro-ph/0206256] [INSPIRE].
- [24] SDSS collaboration, M. Tegmark et al., The 3D power spectrum of galaxies from the SDSS, Astrophys. J. 606 (2004) 702 [astro-ph/0310725] [INSPIRE].
- [25] SDSS collaboration, M. Tegmark et al., Cosmological parameters from SDSS and WMAP, Phys. Rev. D 69 (2004) 103501 [astro-ph/0310723] [INSPIRE].
- [26] D.W. Hogg et al., Cosmic homogeneity demonstrated with luminous red galaxies, Astrophys. J. **624** (2005) 54 [astro-ph/0411197] [INSPIRE].
- [27] A.G. Sanchez et al., Cosmological parameters from CMB measurements and the final 2dFGRS power spectrum, Mon. Not. Roy. Astron. Soc. 366 (2006) 189 [astro-ph/0507583] [INSPIRE].
- [28] SDSS collaboration, M. Tegmark et al., Cosmological constraints from the SDSS luminous red galaxies, Phys. Rev. D 74 (2006) 123507 [astro-ph/0608632] [INSPIRE].
- [29] 2DFGRS collaboration, S. Cole et al., The 2dF galaxy redshift survey: power-spectrum analysis of the final dataset and cosmological implications, Mon. Not. Roy. Astron. Soc. 362 (2005) 505 [astro-ph/0501174] [INSPIRE].
- [30] SDSS collaboration, D.J. Eisenstein et al., Detection of the baryon acoustic peak in the large-scale correlation function of SDSS luminous red galaxies, Astrophys. J. 633 (2005) 560 [astro-ph/0501171] [INSPIRE].
- [31] J. Magorrian et al., The demography of massive dark objects in galaxy centers, Astron. J. 115 (1998) 2285 [astro-ph/9708072] [INSPIRE].
- [32] D. Richstone et al., Supermassive black holes and the evolution of galaxies, Nature **395** (1998) A14 [astro-ph/9810378] [INSPIRE].
- [33] L. Ferrarese and D. Merritt, A fundamental relation between supermassive black holes and their host galaxies, Astrophys. J. **539** (2000) L9 [astro-ph/0006053] [INSPIRE].
- [34] K. Gebhardt et al., A relationship between nuclear black hole mass and galaxy velocity dispersion, Astrophys. J. 539 (2000) L13 [astro-ph/0006289] [INSPIRE].
- [35] S.M. Croom et al., The 2dF QSO redshift survey 12. The spectroscopic catalogue and luminosity function, Mon. Not. Roy. Astron. Soc. **349** (2004) 1397 [astro-ph/0403040] [INSPIRE].
- [36] SDSS collaboration, G.T. Richards et al., Spectroscopic target selection in the Sloan Digital Sky Survey: the quasar sample, Astron. J. 123 (2002) 2945 [astro-ph/0202251] [INSPIRE].
- [37] SDSS collaboration, D.P. Schneider et al., The Sloan Digital Sky Survey quasar catalog V. Seventh data release, Astron. J. 139 (2010) 2360 [arXiv:1004.1167] [INSPIRE].
- [38] F. Hoyle et al., The 2df qso redshift survey VII. constraining cosmology from redshift space distortions via  $\xi(\sigma, \pi)$ , Mon. Not. Roy. Astron. Soc. **332** (2002) 311 [astro-ph/0107348] [INSPIRE].
- [39] P.J. Outram et al., The 2df QSO redshift survey. 11. The QSO power spectrum, Mon. Not. Roy. Astron. Soc. 342 (2003) 483 [astro-ph/0302280] [INSPIRE].
- [40] P.J. Outram et al., The 2dF QSO redshift survey. 13. A measurement of Λ from the QSO power spectrum, Mon. Not. Roy. Astron. Soc. 348 (2004) 745 [astro-ph/0310873] [INSPIRE].

- [41] S.M. Croom et al., The 2dF QSO Redshift Survey. 14. Structure and evolution from the two-point correlation function, Mon. Not. Roy. Astron. Soc. **356** (2005) 415 [astro-ph/0409314] [INSPIRE].
- [42] A.D. Myers, R.J. Brunner, R.C. Nichol, G.T. Richards, D.P. Schneider and N.A. Bahcall, Clustering analyses of 300,000 photometrically classified quasars I. Luminosity and redshift evolution in quasar bias, Astrophys. J. 658 (2007) 85 [astro-ph/0612190] [INSPIRE].
- [43] A.D. Myers et al., Clustering analyses of 300,000 photometrically classified quasars II. The excess on very small scales, Astrophys. J. 658 (2007) 99 [astro-ph/0612191] [INSPIRE].
- [44] A.L. Coil, J.F. Hennawi, J.A. Newman, M.C. Cooper and M. Davis, *The DEEP2 galaxy redshift survey: clustering of quasars and galaxies at* z=1, *Astrophys. J.* **654** (2006) 115 [astro-ph/0607454] [INSPIRE].
- [45] Y. Shen et al., Clustering of high redshift  $(Z \ge 2.9)$  quasars from the Sloan Digital Sky Survey, Astron. J. 133 (2007) 2222 [astro-ph/0702214] [INSPIRE].
- [46] N.P. Ross et al., Clustering of low-redshift ( $z \le 2.2$ ) quasars from the Sloan Digital Sky Survey, Astrophys. J. **697** (2009) 1634 [arXiv:0903.3230] [INSPIRE].
- [47] Y. Shen et al., Quasar clustering from SDSS DR5: dependences on physical properties, Astrophys. J. 697 (2009) 1656 [arXiv:0810.4144] [INSPIRE].
- [48] M. White et al., The clustering of intermediate redshift quasars as measured by the Baryon Oscillation Spectroscopic Survey, Mon. Not. Roy. Astron. Soc. 424 (2012) 933 [arXiv:1203.5306] [INSPIRE].
- [49] S. Eftekharzadeh et al., Clustering of intermediate redshift quasars using the final SDSS III-BOSS sample, Mon. Not. Roy. Astron. Soc. 453 (2015) 2779 [arXiv:1507.08380] [INSPIRE].
- [50] C. Conroy and M. White, A simple model for quasar demographics, Astrophys. J. **762** (2013) 70 [arXiv:1208.3198] [INSPIRE].
- [51] M. Krumpe, T. Miyaji, A.L. Coil and H. Aceves, The spatial clustering of ROSAT all-sky survey AGNs III. Expanded sample and comparison with optical AGNs, Astrophys. J. 746 (2012) 1 [arXiv:1110.5648] [INSPIRE].
- [52] M. Krumpe, T. Miyaji, B. Husemann, N. Fanidakis, A.L. Coil and H. Aceves, The spatial clustering of ROSAT all-sky survey active galactic nuclei IV. More massive black holes reside in more massive dark matter halos, Astrophys. J. 815 (2015) 21 [arXiv:1509.01261] [INSPIRE].
- [53] V. Allevato, A. Finoguenov and N. Cappelluti, Clustering of γ-ray selected 2LAC Fermi blazars, Astrophys. J. 797 (2014) 96 [arXiv:1410.0358] [INSPIRE].
- [54] V. Allevato et al., Clustering of moderate luminosity X-ray-selected Type 1 and Type 2 AGNs at  $z \sim 3$ , Astrophys. J. **796** (2014) 4 [arXiv:1409.7693] [INSPIRE].
- [55] A. Georgakakis et al., Large-scale clustering measurements with photometric redshifts: comparing the dark matter haloes of X-ray AGN, star-forming and passive galaxies at  $z \approx 1$ , Mon. Not. Roy. Astron. Soc. 443 (2014) 3327 [arXiv:1407.1863] [INSPIRE].
- [56] R.C. Hickox et al., Black hole variability and the star formation-active galactic nucleus connection: do all star-forming galaxies host an active galactic nucleus?, Astrophys. J. 782 (2014) 9 [arXiv:1306.3218] [INSPIRE].
- [57] M.A. DiPompeo, A.D. Myers, R.C. Hickox, J.E. Geach and K.N. Hainline, The angular clustering of infrared-selected obscured and unobscured quasars, Mon. Not. Roy. Astron. Soc. 442 (2014) 3443 [arXiv:1406.0778] [INSPIRE].

- [58] M.A. DiPompeo et al., Weighing obscured and unobscured quasar hosts with the cosmic microwave background, Mon. Not. Roy. Astron. Soc. 446 (2015) 3492 [arXiv:1411.0527] [INSPIRE].
- [59] M.A. DiPompeo, J.C. Runnoe, R.C. Hickox, A.D. Myers and J.E. Geach, The impact of the dusty torus on obscured quasar halo mass measurements, Mon. Not. Roy. Astron. Soc. 460 (2016) 175 [arXiv:1604.06811] [INSPIRE].
- [60] A.J. Mendez et al., PRIMUS + DEEP2: clustering of X-ray, radio and IR-AGN at  $z \sim 0.7$ , Astrophys. J. 821 (2016) 55 [arXiv:1504.06284] [INSPIRE].
- [61] A.J. Ross et al., Ameliorating systematic uncertainties in the angular clustering of galaxies: a study using SDSS-III, Mon. Not. Roy. Astron. Soc. 417 (2011) 1350 [arXiv:1105.2320] [INSPIRE].
- [62] BOSS collaboration, A.J. Ross et al., The clustering of galaxies in the SDSS-III Baryon Oscillation Spectroscopic Survey: analysis of potential systematics, Mon. Not. Roy. Astron. Soc. 424 (2012) 564 [arXiv:1203.6499] [INSPIRE].
- [63] BOSS collaboration, A.J. Ross et al., The clustering of galaxies in the completed SDSS-III Baryon Oscillation Spectroscopic Survey: Observational systematics and baryon acoustic oscillations in the correlation function, Mon. Not. Roy. Astron. Soc. 464 (2017) 1168
  [arXiv:1607.03145] [INSPIRE].
- [64] A.D. Myers et al., First measurement of the clustering evolution of photometrically-classified quasars, Astrophys. J. 638 (2006) 622 [astro-ph/0510371] [INSPIRE].
- [65] B. Leistedt, H.V. Peiris, D.J. Mortlock, A. Benoit-Lévy and A. Pontzen, Estimating the large-scale angular power spectrum in the presence of systematics: a case study of Sloan Digital Sky Survey quasars, Mon. Not. Roy. Astron. Soc. 435 (2013) 1857 [arXiv:1306.0005] [INSPIRE].
- [66] B. Leistedt and H.V. Peiris, Exploiting the full potential of photometric quasar surveys: optimal power spectra through blind mitigation of systematics, Mon. Not. Roy. Astron. Soc. 444 (2014) 2 [arXiv:1404.6530] [INSPIRE].
- [67] N. Agarwal et al., Characterizing unknown systematics in large scale structure surveys, JCAP 04 (2014) 007 [arXiv:1309.2954] [INSPIRE].
- [68] M.A. DiPompeo, R.C. Hickox and A.D. Myers, Updated measurements of the dark matter halo masses of obscured quasars with improved WISE and Planck data, Mon. Not. Roy. Astron. Soc. 456 (2016) 924 [arXiv:1511.04469] [INSPIRE].
- [69] P. Laurent et al., A 14  $h^{-3}$  Gpc<sup>3</sup> study of cosmic homogeneity using BOSS DR12 quasar sample, JCAP 11 (2016) 060 [arXiv:1602.09010] [INSPIRE].
- [70] SDSS collaboration, D.J. Eisenstein et al., SDSS-III: massive spectroscopic surveys of the distant universe, the Milky Way galaxy and extra-solar planetary systems, Astron. J. 142 (2011) 72 [arXiv:1101.1529] [INSPIRE].
- [71] L. Anderson et al., The clustering of galaxies in the SDSS-III Baryon Oscillation Spectroscopic Survey: baryon acoustic oscillations in the Data Release 9 spectroscopic galaxy sample, Mon. Not. Roy. Astron. Soc. 427 (2013) 3435 [arXiv:1203.6594] [INSPIRE].
- [72] BOSS collaboration, L. Anderson et al., The clustering of galaxies in the SDSS-III Baryon Oscillation Spectroscopic Survey: baryon acoustic oscillations in the Data Releases 10 and 11 galaxy samples, Mon. Not. Roy. Astron. Soc. 441 (2014) 24 [arXiv:1312.4877] [INSPIRE].
- [73] L. Anderson et al., The clustering of galaxies in the SDSS-III Baryon Oscillation Spectroscopic Survey: measuring D<sub>A</sub> and H at z = 0.57 from the baryon acoustic peak in the Data Release 9 spectroscopic Galaxy sample, Mon. Not. Roy. Astron. Soc. 439 (2014) 83 [arXiv:1303.4666] [INSPIRE].

- [74] A. Slosar et al., The Lyman-alpha forest in three dimensions: measurements of large scale flux correlations from BOSS 1st-year data, JCAP 09 (2011) 001 [arXiv:1104.5244] [INSPIRE].
- [75] A. Slosar et al., Measurement of Baryon Acoustic Oscillations in the Lyman-α forest fluctuations in BOSS data release 9, JCAP 04 (2013) 026 [arXiv:1301.3459] [INSPIRE].
- [76] N.G. Busca et al., Baryon Acoustic Oscillations in the Ly-α forest of BOSS quasars, Astron. Astrophys. 552 (2013) A96 [arXiv:1211.2616] [INSPIRE].
- [77] BOSS collaboration, A. Font-Ribera et al., Quasar-Lyman α forest cross-correlation from BOSS DR11: baryon acoustic oscillations, JCAP 05 (2014) 027 [arXiv:1311.1767] [INSPIRE].
- [78] BOSS collaboration, T. Delubac et al., Baryon acoustic oscillations in the Lyα forest of BOSS DR11 quasars, Astron. Astrophys. 574 (2015) A59 [arXiv:1404.1801] [INSPIRE].
- [79] G.-B. Zhao et al., The extended Baryon Oscillation Spectroscopic Survey: a cosmological forecast, Mon. Not. Roy. Astron. Soc. 457 (2016) 2377 [arXiv:1510.08216] [INSPIRE].
- [80] SDSS collaboration, A. Prakash et al., The SDSS-IV extended Baryonic Oscillation Spectroscopic Survey: luminous red galaxy target selection, Astrophys. J. Suppl. 224 (2016) 34 [arXiv:1508.04478] [INSPIRE].
- [81] EBOSS collaboration, J. Comparat et al., SDSS-IV eBOSS emission-line galaxy pilot survey, Astron. Astrophys. **592** (2016) A121 [arXiv:1509.05045] [INSPIRE].
- [82] A. Raichoor et al., The SDSS-IV extended Baryon Oscillation Spectroscopic Survey: selecting emission line galaxies using the Fisher discriminant, Astron. Astrophys. **585** (2016) A50 [arXiv:1505.01797].
- [83] BOSS collaboration, A.D. Myers et al., The SDSS-IV extended Baryon Oscillation Spectroscopic Survey: quasar target selection, Astrophys. J. Suppl. 221 (2015) 27 [arXiv:1508.04472] [INSPIRE].
- [84] N. Palanque-Delabrouille et al., The extended Baryon Oscillation Spectroscopic Survey: variability selection and quasar luminosity function, Astron. Astrophys. 587 (2016) A41 [arXiv:1509.05607] [INSPIRE].
- [85] S.A. Rodríguez-Torres et al., Clustering of quasars in the First Year of the SDSS-IV eBOSS survey: interpretation and halo occupation distribution, Mon. Not. Roy. Astron. Soc. 468 (2017) 728 [arXiv:1612.06918] [INSPIRE].
- [86] S. Smee et al., The multi-object, fiber-fed spectrographs for SDSS and the Baryon Oscillation Spectroscopic Survey, Astron. J. 146 (2013) 32 [arXiv:1208.2233] [INSPIRE].
- [87] SDSS collaboration, J.E. Gunn et al., The 2.5m telescope of the Sloan Digital Sky Survey, Astron. J. 131 (2006) 2332 [astro-ph/0602326] [INSPIRE].
- [88] J. Bovy, D.W. Hogg and S.T. Roweis, Extreme deconvolution: inferring complete distribution functions from noisy, heterogeneous and incomplete observations, Ann. Appl. Stat. 5 (2011) 1657 [arXiv:0905.2979] [INSPIRE].
- [89] J. Bovy et al., Think outside the color-box: probabilistic target selection and the SDSS-XDQSO quasar targeting catalog, Astrophys. J. 729 (2011) 141 [arXiv:1011.6392] [INSPIRE].
- [90] J. Bovy et al., Photometric redshifts and quasar probabilities from a single, data-driven generative model, Astrophys. J. 749 (2012) 41 [arXiv:1105.3975] [INSPIRE].
- [91] M. Fukugita, T. Ichikawa, J.E. Gunn, M. Doi, K. Shimasaku and D.P. Schneider, The Sloan Digital Sky Survey photometric system, Astron. J. 111 (1996) 1748 [INSPIRE].
- [92] D.P. Finkbeiner et al., Hypercalibration: a Pan-STARRS1-based recalibration of the Sloan Digital Sky Survey photometry, Astrophys. J. 822 (2016) 66 [arXiv:1512.01214].
- [93] E.L. Wright et al., The Wide-field Infrared Survey Explorer (WISE): mission description and initial on-orbit performance, Astron. J. 140 (2010) 1868 [arXiv:1008.0031] [INSPIRE].

- [94] L. Anderson et al., The clustering of galaxies in the SDSS-III Baryon Oscillation Spectroscopic Survey: baryon acoustic oscillations in the Data Release 9 spectroscopic galaxy sample, Mon. Not. Roy. Astron. Soc. 427 (2013) 3435 [arXiv:1203.6594] [INSPIRE].
- [95] D. Bianchi and W.J. Percival, Unbiased clustering estimation in the presence of missing observations, arXiv:1703.02070 [INSPIRE].
- [96] M.E.C. Swanson, M. Tegmark, A.J.S. Hamilton and J.C. Hill, Methods for rapidly processing angular masks of next-generation galaxy surveys, Mon. Not. Roy. Astron. Soc. 387 (2008) 1391 [arXiv:0711.4352] [INSPIRE].
- [97] S.D. Landy and A.S. Szalay, Bias and variance of angular correlation functions, Astrophys. J. 412 (1993) 64 [INSPIRE].
- [98] B. Reid et al., SDSS-III Baryon Oscillation Spectroscopic Survey Data Release 12: galaxy target selection and large scale structure catalogues, Mon. Not. Roy. Astron. Soc. 455 (2016) 1553 [arXiv:1509.06529] [INSPIRE].
- [99] M. White, J.L. Tinker and C.K. McBride, Mock galaxy catalogues using the quick particle mesh method, Mon. Not. Roy. Astron. Soc. 437 (2014) 2594 [arXiv:1309.5532] [INSPIRE].
- [100] I. Pâris et al., The Sloan Digital Sky Survey quasar catalog: twelfth data release, Astron. Astrophys. 597 (2017) A79 [arXiv:1608.06483] [INSPIRE].
- [101] A. Lewis, A. Challinor and A. Lasenby, Efficient computation of CMB anisotropies in closed FRW models, Astrophys. J. 538 (2000) 473 [astro-ph/9911177] [INSPIRE].
- [102] N. Kaiser, Clustering in real space and in redshift space, Mon. Not. Roy. Astron. Soc. 227 (1987) 1 [INSPIRE].
- [103] F. James, MINUIT function minimization and error analysis: reference manual version 94.1, (1994).
- [104] P. Martini and D.H. Weinberg, Quasar clustering and the lifetime of quasars, Astrophys. J. 547 (2001) 12 [astro-ph/0002384] [INSPIRE].
- [105] N. Kaiser, On the spatial correlations of Abell clusters, Astrophys. J. 284 (1984) L9 [INSPIRE].
- [106] J.L. Tinker et al., The large scale bias of dark matter halos: numerical calibration and model tests, Astrophys. J. 724 (2010) 878 [arXiv:1001.3162] [INSPIRE].
- [107] S. Cole and N. Kaiser, Biased clustering in the cold dark matter cosmogony, Mon. Not. Roy. Astron. Soc. 237 (1989) 1127 [INSPIRE].
- [108] Z. Haiman and L. Hui, Constraining the lifetime of quasars from their spatial clustering, Astrophys. J. 547 (2001) 27 [astro-ph/0002190] [INSPIRE].
- [109] J.S.B. Wyithe and A. Loeb, Calibrating the galaxy halo Black hole relation based on the clustering of quasars, Astrophys. J. 621 (2005) 95 [astro-ph/0403714] [INSPIRE].
- [110] J.L. Tinker et al., Toward a halo mass function for precision cosmology: the Limits of universality, Astrophys. J. 688 (2008) 709 [arXiv:0803.2706] [INSPIRE].
- [111] S.M. Croom et al., The 2dF QSO redshift survey 12. The spectroscopic catalogue and luminosity function, Mon. Not. Roy. Astron. Soc. **349** (2004) 1397 [astro-ph/0403040] [INSPIRE].
- [112] S.M. Croom et al., The 2dF QSO redshift survey. 14. Structure and evolution from the two-point correlation function, Mon. Not. Roy. Astron. Soc. 356 (2005) 415 [astro-ph/0409314] [INSPIRE].
- [113] SLOAN DIGITAL SKY SURVEY collaboration, D.P. Schneider et al., *The Sloan Digital Sky Survey Quasar Catalog. 4. Fifth Data Release*, *Astron. J.* **134** (2007) 102 [arXiv:0704.0806] [INSPIRE].

- [114] N.P. Ross et al., Clustering of low-redshift ( $z \le 2.2$ ) quasars from the Sloan Digital Sky Survey, Astrophys. J. **697** (2009) 1634 [arXiv:0903.3230] [INSPIRE].
- [115] A. Font-Ribera et al., The large-scale Quasar-Lyman  $\alpha$  forest cross-correlation from BOSS, JCAP **05** (2013) 018 [arXiv:1303.1937] [INSPIRE].
- [116] P.F. Hopkins et al., The co-formation of spheroids and quasars traced in their clustering, Astrophys. J. 662 (2007) 110 [astro-ph/0611792] [INSPIRE].
- [117] SDSS collaboration, G.T. Richards et al., The Sloan Digital Sky Survey quasar survey: quasar luminosity function from Data Release 3, Astron. J. 131 (2006) 2766 [astro-ph/0601434] [INSPIRE].
- [118] F. Shankar, D.H. Weinberg and J. Miralda-Escude, Self-consistent models of the AGN and black hole populations: duty cycles, accretion rates and the mean radiative efficiency, Astrophys. J. 690 (2009) 20 [arXiv:0710.4488] [INSPIRE].
- [119] Y. Shen et al., Cross-correlation of SDSS DR7 Quasars and DR10 BOSS galaxies: the weak luminosity dependence of quasar clustering at  $z \sim 0.5$ , Astrophys. J. 778 (2013) 98 [arXiv:1212.4526] [INSPIRE].
- [120] A.G. Krolewski and D.J. Eisenstein, Measuring the luminosity and virial black hole mass dependence of quasar-galaxy clustering at  $z \sim 0.8$ , Astrophys. J. 803 (2015) 4 [arXiv:1501.03898] [INSPIRE].